

Krylov Complexity of Supersymmetric SYK Models

James Chryssanthacopoulos, David Vegh

*Centre for Theoretical Physics, Department of Physics and Astronomy
Queen Mary University of London, 327 Mile End Road, London E1 4NS, UK*

Email: j.chryssanthacopoulos@qmul.ac.uk, d.vegh@qmul.ac.uk

Abstract

We study the effect of supersymmetry breaking on Krylov complexity in the $\mathcal{N} = 2$ SYK model under irrelevant and mass deformations of the Hamiltonian. The irrelevant deformation breaks $\mathcal{N} = 2$ supersymmetry down to $\mathcal{N} = 1$, while the mass deformation breaks supersymmetry completely. Using Krylov subspace methods, we analyze the Lanczos sequence, Krylov dimension, complexity, and entropy at finite system size as functions of deformation strength. Both deformations enlarge the Krylov space, but the mass deformation has a stronger effect. Krylov complexity exhibits initial quadratic growth, followed by linear growth across both deformations. We observe that both deformations increase the quadratic and linear growth rates of Krylov complexity at early times. At late times, the irrelevant deformation increases the saturation complexity as a fraction of the Krylov dimension, while the mass deformation decreases it. This reveals distinct signatures of how supersymmetry breaking impacts quantum complexity.

Contents

1	Introduction	1
2	Supersymmetric SYK Models	2
2.1	$\mathcal{N} = 0$ SYK	3
2.2	$\mathcal{N} = 1, 2$ SYK	5
2.3	Deformations	7
3	Krylov Complexity and the SYK Model	9
3.1	Krylov Space	10
3.2	Krylov Dimension	13
3.3	Krylov Complexity and Entropy	14
4	Results	15
4.1	Krylov Dimension	15
4.2	Lanczos Sequence	17
4.3	Krylov Complexity and Entropy	20
5	Discussion	24
A	Complexity Results for Different System Sizes	27
B	Comparison of Different Lanczos Algorithms	31
C	Estimation of Krylov Complexity Parameters	33

1 Introduction

Krylov complexity has recently emerged as a powerful tool for studying quantum chaos in many-body quantum systems and gravity [1–3]. Roughly, Krylov complexity measures how quickly an operator grows under generic Hamiltonian evolution. In a chaotic system, Krylov complexity typically grows exponentially at early times, which provides a useful probe of quantum chaos. The notion of Krylov complexity grew out of a need to understand quantum chaos beyond the semiclassical limit. Semiclassically, chaos is often diagnosed through the Lyapunov exponent, which quantifies the exponential growth of out-of-time-order correlators. The Lyapunov exponent is bounded by the temperature of the system, and maximally chaotic systems, such as black holes, saturate this bound [4, 5]. Krylov complexity extends this idea to more general settings, quantifying operator growth under generic, non-integrable Hamiltonian dynamics. When the Lyapunov exponent can be defined, it is bounded by the exponential growth rate of Krylov complexity [6].

The fundamental idea behind Krylov complexity, and Krylov subspace methods generally, is to identify a minimal subspace in which an operator evolves [7]. This subspace is constructed by means of the Lanczos algorithm [8]. In this algorithm, an initial operator is evolved using the Liouvillian, the generator of time evolution. After each step, the overlap with all previous operators is subtracted in a Gram-Schmidt-like procedure. The resulting orthonormal basis is called the Krylov basis. In addition to the Krylov basis, the Lanczos algorithm generates a sequence of coefficients, called the Lanczos coefficients, which correspond to the size of the Krylov basis elements. In a chaotic system, the Lanczos coefficients initially grow in a system-dependent way before entering a regime of linear growth at intermediate times. The coefficients then plateau and finally decay [6]. The Lanczos sequence captures the complete system dynamics, from which Krylov complexity can be computed.

One interesting model which has been used to study Krylov complexity is the Sachdev-Ye-Kitaev (SYK) model, a quantum mechanical model of interacting fermions with random couplings [9–15]. Because its Lyapunov exponent saturates the bound, the SYK model is maximally chaotic and has been proposed as a simple, one-dimensional model of quantum black holes. At low energies, SYK exhibits emergent conformal symmetry. In the soft sector, the model can be described holographically by Jackiw-Teitelboim (JT) gravity, a two-dimensional gravitational theory in anti-de Sitter space [16–19]. The Lanczos sequence of the model was shown to exhibit initial linear growth characteristic of chaotic systems [6]. Krylov complexity also grows exponentially at early times. When the number of interactions is large, the exponential growth rate of Krylov complexity matches the Lyapunov exponent, again suggesting maximal chaos.

One major way to generalize the SYK model is to introduce supersymmetry, which can be used to study supersymmetric black holes [20, 21]. There are different versions of supersymmetric SYK depending on the number of supercharges. Roughly, supersymmetric SYK models possess the same form as their non-supersymmetric counterparts, but the couplings are no longer independent. These correlations change the structure of the large- N equations and the conformal dimension of the fermions, but generally the models are maximally chaotic in the sense that their Lyapunov exponents saturate the bound [22]. Starting at $\mathcal{N} = 2$, which possesses two complex supercharges, the model develops a large degeneracy of ground states with exactly zero energy, called BPS states [23, 24]. Between the discrete BPS states and non-BPS continuum, there is a gap of order $1/S$, where S is the entropy. Because of its interesting properties, $\mathcal{N} = 2$ SYK has been used to study the thermodynamics of extremal, supersymmetric black holes in higher dimensions.

Although the Lyapunov exponent of supersymmetric SYK in the large- N limit has been studied extensively, Krylov complexity of supersymmetric SYK has received less attention. A study of Krylov complexity of $\mathcal{N} = 1$ SYK has been conducted, but it was embedded within a larger study of $T\bar{T}$ -deformed SYK that also analyzed other measures of chaos [25]. The chaotic properties of

$\mathcal{N} = 2$ have also been studied, but primarily within the context of random matrix theory [26]. The related concept of spread complexity has also been applied to supersymmetric systems, but not to $\mathcal{N} = 2$ SYK [27]. This paper is devoted to a thorough study of Krylov complexity of the $\mathcal{N} = 2$ SYK model. Various deformations are explored that break the supersymmetry, which enable the effects of supersymmetry on Krylov complexity to be studied.

The first deformation that is treated is a UV deformation introduced in [23]. Because this deformation is irrelevant, it does not spoil the IR physics, which corresponds to the gravitational dynamics. The deformation breaks $\mathcal{N} = 2$ down to $\mathcal{N} = 1$, eliminating the BPS states and lifting the ground-state degeneracy for even parametrically small values of the deformation parameter. This deformation can be seen as interpolating between two types of black holes [28, 29]. The first corresponds to extremal, supersymmetric black holes which carry a large entropy reflecting the ground-state degeneracy. The second type of black hole corresponds to near-extremal, non-supersymmetric black holes which display no ground-state degeneracy and an average energy spacing that is exponentially suppressed in the entropy.

While the UV deformation is interesting on the level of black hole physics, this paper studies the effect of the deformation on Krylov complexity at finite N and infinite temperature. Some relevant questions include the following. How does supersymmetry breaking alter the Lanczos sequence? How do the coefficients grow initially? How do the sequences compare across different operators and system sizes? How does Krylov complexity respond to the deformation? Does it grow exponentially at early times, or does it follow another growth profile? These questions will be answered numerically, which presents significant computational challenges. These challenges include the exponential growth of the Hilbert space with system size and the breakdown of orthogonality in the Krylov basis as the number of iterations increases. Addressing these challenges necessitates the use of optimized, parallelized implementations of the Lanczos algorithm.

The second deformation that is explored is a relevant deformation that corresponds on the gravity side to deformations away from two-dimensional anti-de Sitter space. There are many types of relevant deformations that can be considered, but one of the simplest involves adding the Hamiltonian of two-body SYK with complex fermions, which is a free, integrable theory [30, 31]. This mass deformation provides another pattern of supersymmetry breaking that breaks $\mathcal{N} = 2$ directly down to $\mathcal{N} = 0$. The BPS degeneracy is lifted, and the energies are no longer bounded from below by zero. The incorporation of an integrable Hamiltonian helps steer the model toward integrability, which has a direct bearing on Krylov complexity that distinguishes between chaotic and integrable dynamics [32–34]. The same types of questions as before will be addressed.

The remainder of this paper is organized as follows. In Section 2, supersymmetric SYK models are reviewed, focusing on $\mathcal{N} = 2$ and its symmetries. Section 3 reviews Krylov complexity, including the Lanczos algorithm. In Section 4, numerical results are presented for the Krylov dimension, Lanczos sequence, and Krylov complexity and entropy for the different deformations and several initial operators. Section 5 concludes with a discussion of findings and suggestions for future work.

2 Supersymmetric SYK Models

This section provides the necessary background for understanding supersymmetric SYK. Section 2.1 reviews non-supersymmetric, or $\mathcal{N} = 0$, SYK, including its symmetries and spectral properties. Then Section 2.2 reviews SYK models with $\mathcal{N} = 1$ and $\mathcal{N} = 2$ supersymmetry. Section 2.3 introduces the deformations of the models which are relevant for the rest of the paper.

2.1 $\mathcal{N} = 0$ SYK

Before introducing supersymmetric SYK, it is useful to review the basic properties of the regular SYK model, or $\mathcal{N} = 0$ SYK. The SYK model is a $(0 + 1)$ -dimensional quantum mechanical model of N fermions with random interactions. Each of the fermions can interact with any of the others, but only q of them interact at a time, with q even. There are two versions of $\mathcal{N} = 0$ SYK, one with Majorana fermions and another with Dirac fermions. In the Majorana version, the Hamiltonian is given by

$$H = i^{\frac{q}{2}} \sum_{1 \leq i_1 < \dots < i_q \leq N} J_{i_1 \dots i_q} \psi_{i_1} \dots \psi_{i_q} \quad (2.1)$$

where ψ_i satisfy the algebra $\{\psi_i, \psi_j\} = \delta_{ij}$. The couplings $J_{i_1 \dots i_q}$ are drawn from a Gaussian distribution with zero mean and variance

$$\langle J_{i_1 \dots i_q}^2 \rangle = \frac{J^2(q-1)!}{N^{q-1}} \quad (2.2)$$

The parameter J is a dimension-one parameter controlling the interaction strength. The various numerical factors and powers of N are introduced to simplify the large- N limit. The factor $i^{\frac{q}{2}}$ is included to ensure the Hamiltonian is Hermitian.

At finite N , one way to study the SYK model is to construct the Hamiltonian explicitly in some basis and diagonalize it. For even N , the model can be implemented using $N/2$ Dirac fermions c_i . These Dirac fermions map to Majorana fermions in pairs:

$$\psi_{2i-1} = \frac{i(c_i - c_i^\dagger)}{\sqrt{2}}, \quad \psi_{2i} = \frac{c_i + c_i^\dagger}{\sqrt{2}} \quad (2.3)$$

where $\{c_i, c_j^\dagger\} = \delta_{ij}$ and $\{c_i, c_j\} = \{c_i^\dagger, c_j^\dagger\} = 0$. The total fermion number can be defined as $F \equiv \sum_{i=1}^{N/2} c_i^\dagger c_i$. This is not a conserved charge, but fermion number parity, $F \bmod 2$, is conserved. This entails that the Hamiltonian can be block-diagonalized into sectors of even and odd fermion number [35]. In practice, one way to implement Dirac fermions is by means of the Jordan-Wigner transformation, which maps them to a chain of spin-1/2 particles. The construction is

$$c_i = \prod_{k=1}^{i-1} (-\sigma_k^z) \frac{\sigma_i^x - i\sigma_i^y}{2}, \quad c_i^\dagger = \prod_{k=1}^{i-1} (-\sigma_k^z) \frac{\sigma_i^x + i\sigma_i^y}{2} \quad (2.4)$$

where σ_i^j is the Pauli matrix in the j direction acting on the i th spin. The dimension of the Hilbert space is $2^{N/2}$.

The $\mathcal{N} = 0$ SYK model involving Dirac fermions, called complex SYK, is built in much the same way as the Majorana version [36–39]. This model can be defined for any q -body interaction, but for $q = 4$ the Hamiltonian takes the form

$$H = \sum_{ijkl} J_{ij;kl} c_i^\dagger c_j^\dagger c_k c_l \quad (2.5)$$

where c_i can be constructed from Equation (2.4). The random couplings $J_{ij;kl}$ have the same statistics as in the Majorana case, but are complex-valued. The indices are also divided into two sets, obeying the relations

$$J_{ji;kl} = J_{ij;lk} = -J_{ij;kl}, \quad J_{kl;ij} = J_{ij;kl}^* \quad (2.6)$$

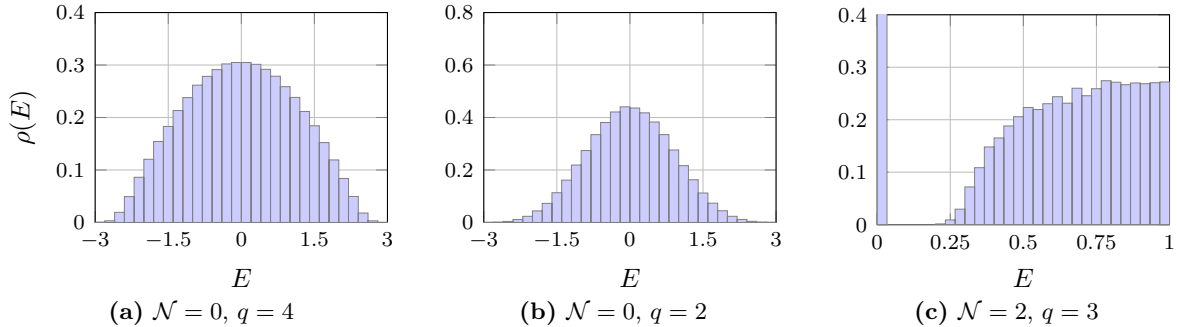


Figure 1: The spectral density $\rho(E)$ for different SYK models. Figure (a) resembles the Wigner semicircle distribution, typical of chaotic systems, while figure (b) resembles a Gaussian, which is characteristic of integrable systems. Figure (c) exhibits a large zero-energy ground state degeneracy and a gap to the first excited state. Each plot corresponds to 500 realizations of the Hamiltonian with $N = 10$, $F = 5$, and $J = 1$.

Because the Hamiltonian is built from complex instead of real fermions, the dimension of the Hilbert space is 2^N instead of $2^{N/2}$.

The complex SYK model possesses a global $U(1)$ symmetry absent in the Majorana model, in which the Hamiltonian is invariant under the transformation $c_i \rightarrow e^{i\alpha}c_i$. This symmetry leads to conservation of the total fermion number F . Because F commutes with the Hamiltonian, the Hamiltonian can be decomposed into sectors of fixed fermion number. This decomposition enables studies of the model in lower-dimensional subspaces, eliminating the need to fully diagonalize the Hamiltonian. In the remainder of this paper, unless otherwise stated, $\mathcal{N} = 0$ SYK will refer to the complex SYK model.

One way of investigating the chaotic properties of the SYK model is to study its energy eigenvalues, or spectral properties. Figure 1(a) shows the spectral density $\rho(E)$ of $\mathcal{N} = 0$ SYK with $q = 4$ interactions. The distribution was obtained by exactly diagonalizing 500 samples of the Hamiltonian. The number of fermions is $N = 10$, and the model was diagonalized in the sector $F = 5$ with $J = 1$. The density resembles the Wigner semicircle distribution, which arises from the eigenvalues of random matrices [40, 41]. The distribution does not peak sharply at $E = 0$ and drops off rapidly at large energies. The shape of the distribution results from repulsion between energy levels, which is characteristic of chaotic systems.

A further way of investigating the spectral properties of the model is to examine the density of spacings between successive eigenvalues $p(s)$, called the level spacings. This is shown in Figure 2(a). Eigenvalue repulsion causes the distribution to peak at $s > 0$. Besides the peak, the gap ratio r is another way of characterizing the level spacing distribution, given by

$$r \equiv \frac{\min(s_i, s_{i+1})}{\max(s_i, s_{i+1})} \quad (2.7)$$

where s_i is the spacing between level i and $i + 1$. For $\mathcal{N} = 0$ with $q = 4$ interactions, the mean gap ratio is $\langle r \rangle \approx 0.60$, which is indicative of eigenvalue repulsion.

It is important to note that the properties of the energy levels depend strongly on the particular sector of fermion number used. At smaller F than the one used here, the effects mentioned above become more pronounced. The characteristic domain of the spectral density narrows, and the level spacing density peaks at larger spacings. For higher values of F , including $F = N$ which corresponds to the full Hilbert space, the energy levels do not repel, and the level spacings peak at $s = 0$. This change in spectral properties is likely due to mixing between various symmetry sectors, which spoils the level repulsion.

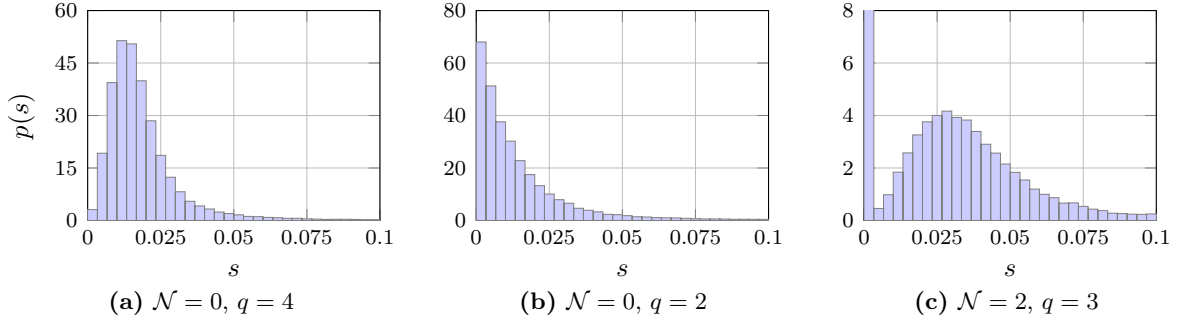


Figure 2: The level spacing density $p(s)$ for different SYK models. Figure (a) is peaked around $s > 0$ because the energy levels repel each other, while figure (b) is a Poisson distribution peaked at $s = 0$. Figure (c) has a peak at $E = 0$ because of the zero-energy degeneracy, but otherwise peaks at $s > 0$ similar to figure (a). Each plot corresponds to 500 realizations of the Hamiltonian with $N = 10$, $F = 5$, and $J = 1$.

A special case of the $\mathcal{N} = 0$ SYK model is when $q = 2$. In this case, the Hamiltonian contains only quadratic terms of the form

$$H = \sum_{ij} J_{ij} c_i^\dagger c_j \quad (2.8)$$

where J_{ij} is a Hermitian matrix whose elements are sampled from a Gaussian distribution with zero mean and variance $J^2/4N$. This model is a free, integrable theory, which can again be seen by studying its spectral properties. Figure 1(b) shows the spectral density for the $q = 2$ model. The distribution is shaped like a Gaussian, peaking sharply at $E = 0$ and tapering off smoothly at large energies. Figure 2(b) shows the distribution of level spacings. Because the eigenvalues do not repel each other, the level spacings follow a Poisson distribution that peaks at $s = 0$, where eigenvalues cluster together. The mean gap ratio is $\langle r \rangle \approx 0.38$, which is characteristic of integrable systems.

2.2 $\mathcal{N} = 1, 2$ SYK

The SYK model can be generalized to include supersymmetry, which can be used to study supersymmetric black holes [20, 22, 26, 42]. There are various types of supersymmetric SYK models corresponding to different numbers of supercharges, but two of the most studied are $\mathcal{N} = 1$ and $\mathcal{N} = 2$. The $\mathcal{N} = 1$ model uses Majorana fermions, while $\mathcal{N} = 2$ uses Dirac fermions. In $\mathcal{N} = 1$, the supercharge Q is defined as

$$Q = i^{\frac{q-1}{2}} \sum_{1 \leq i_1 < \dots < i_q \leq N} C_{i_1 i_2 \dots i_q} \psi_{i_1} \psi_{i_2} \dots \psi_{i_q} \quad (2.9)$$

where ψ_i are Majorana fermions and q is taken to be odd. The variance of the couplings $C_{i_1 \dots i_q}$ is the same as in Equation (2.2). The supercharge is the generator of supersymmetric transformations. The supersymmetric partners of the fermions ψ_i are bosons b_i , which are not dynamical. The Hamiltonian is the square of the supercharge, which simplifies to

$$H = Q^2 = E_0 + \sum_{1 \leq i_1 < \dots < i_{\tilde{q}} \leq N} J_{i_1 \dots i_{\tilde{q}}} \psi_{i_1} \dots \psi_{i_{\tilde{q}}} \quad (2.10)$$

where $\tilde{q} = 2q - 2$ and E_0 is the ground state energy.

At finite N , the $\mathcal{N} = 1$ model has a non-zero ground state energy, which breaks supersymmetry, but it is recovered in the large- N limit [20]. Notice that the Hamiltonian of Equation (2.10) has the

same form as the Hamiltonian of $\mathcal{N} = 0$ Majorana SYK with \tilde{q} interactions, but the couplings $J_{i_1 \dots i_{\tilde{q}}}$ are not independent. Instead, they roughly correspond to the covariance matrix of the couplings $C_{i_1 \dots i_q}$. For $q = 3$, these couplings are given by

$$J_{ijkl} = -\frac{1}{8} \sum_a C_{a[ij} C_{kl]a} \quad (2.11)$$

The second major type of supersymmetric SYK model is the $\mathcal{N} = 2$ model. In the $\mathcal{N} = 2$ model, there are two supercharges, Q and Q^\dagger . The Hamiltonian is given by

$$H = \{Q, Q^\dagger\} \quad (2.12)$$

which has the same form as the Hamiltonian of complex SYK with \tilde{q} interactions, but with couplings that are not fully independent. The supercharges are nilpotent, $Q^2 = Q^{\dagger 2} = 0$, which follows from the anticommutation relation between fermions, $\{c_i, c_j\} = 0$. Because of nilpotency, the Hamiltonian can also be written $H = \{Q, Q^\dagger\} = (Q + Q^\dagger)^2$. The nilpotency of the supercharges also implies supersymmetry:

$$[Q, H] = [Q, \{Q, Q^\dagger\}] = [Q^2, Q^\dagger] = 0 \quad \text{if} \quad Q^2 = 0 \quad (2.13)$$

Similarly, $[Q^\dagger, H] = 0$. To summarize, the fermionic anticommutation relations imply nilpotency of the supercharges, which implements supersymmetry.

Like the complex SYK model, the $\mathcal{N} = 2$ model possesses a global $U(1)$ symmetry, which leads to conservation of total fermion number F . The $\mathcal{N} = 2$ theory possesses an additional $U(1)$ R-symmetry generated by the operator

$$R = \frac{1}{2q} \sum_i [c_i^\dagger, c_i] \quad (2.14)$$

With this definition, the supercharges carry charge ± 1 , while the fermions carry charge $\pm 1/q$. The commutation relations are

$$[R, Q] = -Q, \quad [R, Q^\dagger] = Q^\dagger, \quad [R, c_i] = -\frac{1}{q} c_i, \quad [R, c_i^\dagger] = \frac{1}{q} c_i^\dagger \quad (2.15)$$

While the $U(1)_R$ charge does not commute with the supercharges, there is a Z_q subgroup of this symmetry that does, which transforms the fermions as $c_i \rightarrow e^{\frac{2\pi i n}{q}} c_i$, $n \in \mathbb{Z}_q$ [20].

Because the $U(1)_R$ charge commutes with the Hamiltonian, the Hilbert space can be decomposed as $\mathcal{H} = \bigoplus_k \mathcal{H}_k$, where \mathcal{H}_k is the subspace of states with $U(1)_R$ charge k . In each space \mathcal{H}_k , there are BPS and non-BPS supermultiplets. BPS states are zero-energy states annihilated by the supercharges Q and Q^\dagger [43, 44]. Non-BPS states are raised or lowered to other R -charge sectors by the supercharges. BPS states appear with a large degeneracy at $E = 0$. Non-BPS states exhibit a dense spectrum starting from a non-zero energy.

The spectral density of the $\mathcal{N} = 2$ model with $q = 3$ is shown in Figure 1(c). The distribution has a large degeneracy at exactly zero energy, which corresponds to the BPS states. The number of BPS states is 162, which comprises roughly 16% of all states. The spectrum also exhibits a large gap between the degenerate BPS states and the non-BPS continuum. Figure 2(c) shows the distribution of level spacings for the $\mathcal{N} = 2$ model. The distribution peaks at $s = 0$ because of the large ground state degeneracy. Outside of this sector, the distribution is peaked at $s > 0$, similar to $\mathcal{N} = 0$ SYK with $q = 4$ interactions.

2.3 Deformations

It is possible to study deformations of the supersymmetric SYK model that break supersymmetry. Generally, supersymmetry can be broken by adding any term to the Hamiltonian that is not a square of a supercharge. This paper explores two types of deformations. The first is an irrelevant deformation that does not modify the conformal phase of the theory at low energies, which corresponds to the gravitational sector. The second is a mass deformation which alters the gravitational dynamics and more drastically modifies the chaotic properties of the model.

The first deformation can be implemented by adding UV terms to the Lagrangian. Taken from [23], the deformation is given by

$$\mathcal{L} \rightarrow \mathcal{L} + \epsilon \left(i \sum_i c_i \partial_\tau c_i - \sum_i b_i^2 + \text{h.c.} \right) \quad (2.16)$$

where h.c. denotes the Hermitian conjugate of the terms in parentheses, and ϵ controls the strength of the deformation. One can show that this Lagrangian leads to a Hamiltonian with the same form as before, $H = \{Q, Q^\dagger\}$, with the supercharge Q having the same form as in Equation (2.9), provided the fermions satisfy an ϵ -deformed algebra:

$$\{c_i, c_j^\dagger\} = \frac{1}{1 - \epsilon^2} \delta_{ij}, \quad \{c_i, c_j\} = -\{c_i^\dagger, c_j^\dagger\} = \frac{i\epsilon}{1 - \epsilon^2} \delta_{ij} \quad (2.17)$$

When $\epsilon = \pm 1$, these expressions are singular, due to the presence of fermionic and bosonic zero modes. This restricts ϵ to the range $|\epsilon| < 1$.

Recall that in the $\mathcal{N} = 2$ model, the fermionic anticommutation relation $\{c_i, c_j\} = 0$ led to the nilpotency of the supercharges, which implemented supersymmetry. In the deformed case, $\{c_i, c_j\} \neq 0$, which means the supercharges are no longer nilpotent. The charges no longer commute with the Hamiltonian, breaking supersymmetry, but the sum of the charges $\mathcal{Q} \equiv Q + Q^\dagger$ is still a symmetry as the Hamiltonian can be written $H = \mathcal{Q}^2$. The result is that $\mathcal{N} = 2$ breaks down to $\mathcal{N} = 1$. At finite N , this has the effect of breaking supersymmetry completely, because the $\mathcal{N} = 1$ model has broken supersymmetry outside the large- N limit. The deformation also breaks the global $U(1)$ and $U(1)_R$ symmetries.

Starting from the fermions c_i that satisfy the ϵ -deformed algebra in Equation (2.17), it is possible to introduce a change of basis to bring them into canonical form. This transformation is given by

$$c_i = \frac{\cos \frac{\tilde{\epsilon}}{2}}{\cos \tilde{\epsilon}} \chi_i + i \frac{\sin \frac{\tilde{\epsilon}}{2}}{\cos \tilde{\epsilon}} \chi_i^\dagger \quad (2.18)$$

where $\epsilon = \sin \tilde{\epsilon}$, with $-\pi/2 < \tilde{\epsilon} < \pi/2$. This naturally restricts to $|\epsilon| < 1$. If c_i and c_i^\dagger satisfy the ϵ -deformed algebra, then χ_i and χ_i^\dagger satisfy the canonical fermionic algebra. When $\epsilon \rightarrow 0$, or equivalently $\tilde{\epsilon} \rightarrow 0$, $c_i \rightarrow \chi_i$ and the model reduces to the original $\mathcal{N} = 2$ model. This transformation also provides a prescription for constructing the Hamiltonian starting from canonical fermions. One can generate canonical fermions, apply the transformation of Equation (2.18), then insert the resulting fermions into the supercharge. This supercharge will not be nilpotent. This demonstrates that it is not possible to pick a basis such that Q is holomorphic in the fermion fields and, simultaneously, the fermions satisfy the canonical algebra.

The effect of the deformation can be seen by considering the spectral density as a function of the deformation strength ϵ , shown in the top row of Figure 3. Because the deformation breaks the $U(1)$ symmetry, the Hamiltonian was constructed in the full Hilbert space. The undeformed model has a large sector of degenerate BPS states at $E = 0$ separated by a gap from a continuum of

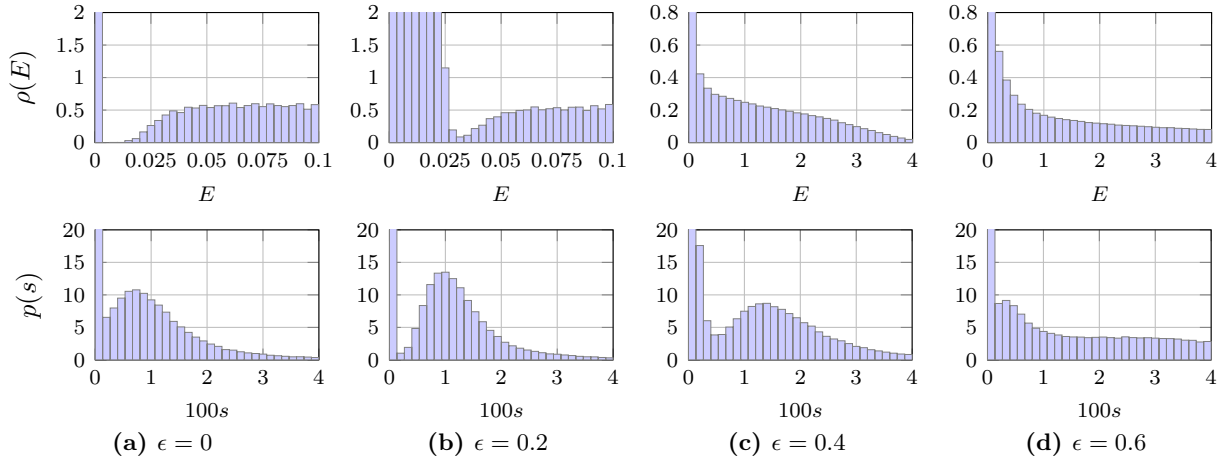


Figure 3: The spectral density $\rho(E)$ and level spacing density $p(s)$ for $\mathcal{N} = 2$ SYK as the strength ϵ of an irrelevant deformation varies. The BPS degeneracy lifts, while the energy gap closes. The level spacings shift to the right before flattening out. Each plot corresponds to 500 realizations of the Hamiltonian with $N = 10$, $q = 3$, and $J = 1$.

non-BPS states. When the deformation is turned on, half of the $\mathcal{N} = 2$ supersymmetry is broken, and the degeneracy starts to lift. The ground state energy increases, but remains positive. At $\epsilon = 0.2$, the average ground state energy is 3.5×10^{-3} , increasing to 8.5×10^{-2} at $\epsilon = 0.6$. The energy gap between BPS and non-BPS states also closes with the deformation. At $\epsilon \approx 0.1$, the gap closes completely. At large values of ϵ , the spectral density peaks at low energies and tapers off smoothly, similar to the $\mathcal{N} = 0$ model with $q = 2$ interactions.

The effect of the deformation can also be witnessed in the level spacings, shown in the bottom row of Figure 3. For small values of the deformation, the lifting of the degeneracy reduces the occurrence of closely spaced energy levels, carving out a section of probability mass at low values of s . Under large deformations, the energy levels simultaneously cluster and repel each other, causing the distribution to become more uniform. Figure 4 shows how the mean gap ratio $\langle r \rangle$ varies with the deformation strength ϵ . To account for the presence of degeneracies, spacings less than 10^{-10} were removed before computing the gap ratio. The undeformed model has $\langle r \rangle \approx 0.48$. As the deformation is turned on, the gap ratio increases, reaching a maximum of $\langle r \rangle \approx 0.67$. This indicates a stronger level repulsion than in the undeformed model.

The second deformation that will be explored is a relevant deformation. Relevant deformations correspond to deformations of the two-dimensional anti-de Sitter vacuum in the gravity picture. Generally, the non-supersymmetric SYK model admits a set of relevant deformations given by

$$H = H_{\mathcal{N}=0}^q + \sum_i \epsilon_i H_{\mathcal{N}=0}^{\tilde{q}_i} \quad (2.19)$$

The Hamiltonian is a sum of multiple Hamiltonians with different numbers of fermions, q and \tilde{q}_i . If $\tilde{q}_i < q$, the second term acts as a relevant deformation controlled by the dimensionless couplings ϵ_i [30, 31, 45]. This picture is modified slightly when moving to the $\mathcal{N} = 2$ model. In this case, a class of relevant deformations can be written

$$H = H_{\mathcal{N}=2}^q + \sum_i \epsilon_i H_{\mathcal{N}=0}^{\tilde{q}_i} \quad (2.20)$$

This Hamiltonian is the sum of the $\mathcal{N} = 2$ Hamiltonian with q interactions and a set of $\mathcal{N} = 0$ Hamiltonians with \tilde{q}_i interactions. In $\mathcal{N} = 2$ SYK, the conformal dimension of the fermions is $1/2q$

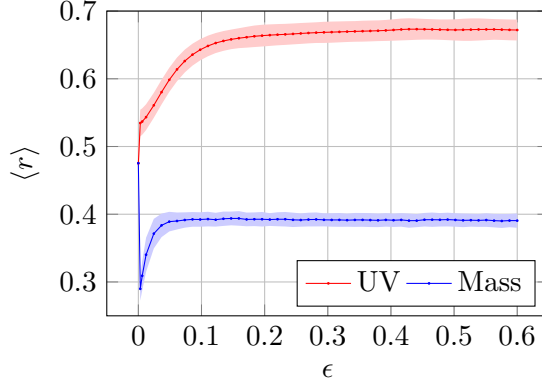


Figure 4: The average gap ratio $\langle r \rangle$ as the strength ϵ of both deformations varies. The undeformed model has $\langle r \rangle \approx 0.48$. The irrelevant deformation increases the gap ratio to a level consistent with chaotic systems. The mass deformation decreases the ratio to a value in line with integrable systems. Each curve corresponds to the average of 500 realizations of the Hamiltonian with $N = 10$, $q = 3$, and $J = 1$. The shaded regions indicate the standard deviation. To account for degeneracies, spacings less than 10^{-10} were discarded.

instead of $1/q$. This means the deformation is relevant if $\tilde{q}_i < 2q$. For the $q = 3$ model considered in this paper, this restricts \tilde{q}_i to two or four. The deformation that will be considered involves a single term with $\tilde{q}_i = 2$ given by

$$H = H_{\mathcal{N}=2}^{q=3} + \epsilon \sum_{ij} J_{ij} c_i^\dagger c_j \quad (2.21)$$

Because the second term corresponds to a free theory, the deformation interpolates between a chaotic and integrable system. Unlike the irrelevant deformation, this deformation preserves various symmetries, including the $U(1)$ symmetry. Note that the ϵ used here is distinct from the one used in the irrelevant deformation. While ϵ of the irrelevant deformation is constrained to lie inside $|\epsilon| < 1$, the ϵ of the mass deformation is valid for all $\epsilon \geq 0$.

The spectral and level spacing densities as a function of the mass deformation strength are shown in Figure 5. Even at small values of the deformation, the BPS degeneracy and energy gap are eliminated. The energy is no longer bounded from below by zero. The level spacing density resembles a Poisson distribution starting at low values of the deformation, and retains its shape for larger values. At higher values of ϵ , the spectral density settles into a Gaussian with positive mean. Figure 4 also shows how the mean gap ratio $\langle r \rangle$ varies with the mass deformation strength ϵ . As soon as the deformation is turned on, the gap ratio drops sharply as the energy gap is eliminated and the spectrum incorporates energy levels from the integrable term. As ϵ increases further, the integrable term becomes more dominant, and the gap ratio increases to $\langle r \rangle \approx 0.39$, consistent with integrable systems.

3 Krylov Complexity and the SYK Model

This section reviews the main ideas behind Krylov complexity and its application to the SYK model. Section 3.1 introduces the notion of Krylov space and discusses how to construct it using the Lanczos algorithm. Then Section 3.2 discusses the size of the Krylov space, called the Krylov dimension, and describes how to obtain bounds on it based on the degeneracies of the energy spectrum. Section 3.3 concludes with a review of Krylov complexity and entropy.

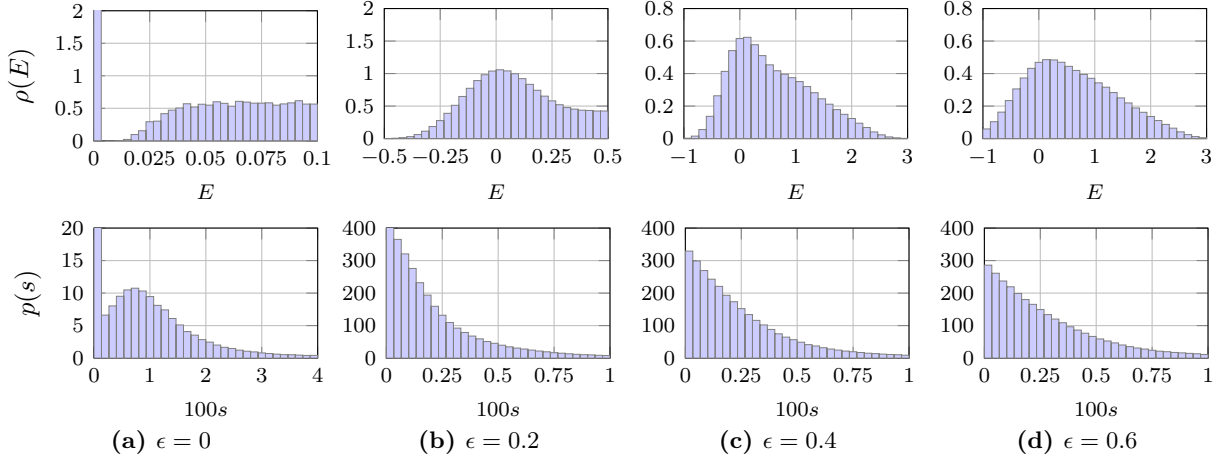


Figure 5: The spectral density $\rho(E)$ and level spacing density $p(s)$ for $\mathcal{N} = 2$ SYK as the strength ϵ of a mass deformation varies. The BPS degeneracy and energy gap are eliminated, and the energy is allowed to go negative. The level spacing density resembles a Poisson distribution when the deformation is turned on. Each plot corresponds to 500 realizations of the Hamiltonian with $N = 10$, $q = 3$, and $J = 1$.

3.1 Krylov Space

Under time evolution by a Hamiltonian, a generic operator will trace out a trajectory in Hilbert space. In many instances, this operator will not explore the entire Hilbert space, but instead will be confined to a subspace. Krylov space is one way of defining this subspace in which the dynamics unfolds [1]. To develop these ideas, consider a Hermitian operator \mathcal{O} evolving in time under the action of a time-independent Hamiltonian H . In the Heisenberg picture, the dynamics of the operator is governed by the equation

$$\partial_t \mathcal{O}(t) = i[H, \mathcal{O}(t)] \equiv i\mathcal{L}\mathcal{O}(t) \quad (3.1)$$

The operator \mathcal{L} is called the Liouvillian superoperator. Its action on an operator is given by the commutator of that operator with the Hamiltonian, $\mathcal{L} \cdot = [H, \cdot]$. The solution to the Heisenberg equation is

$$\mathcal{O}(t) = e^{i\mathcal{L}t} \mathcal{O} \quad (3.2)$$

In words, the operator at time t is obtained by applying powers of the Liouvillian on the initial operator. This evolution is contained in a subspace of operator space, called Krylov space, that is spanned by

$$\text{span}\{\mathcal{L}^n \mathcal{O}\}_{n=0}^{\infty} = \{\mathcal{O}, \mathcal{L}\mathcal{O}, \mathcal{L}^2\mathcal{O}, \dots\} \quad (3.3)$$

The size of this space, called the operator size, grows in time as more terms are needed to describe the operator. Operator size is one way of quantifying how much the operator has spread out in Hilbert space, a phenomenon known as operator scrambling.

To construct the Krylov space, it is convenient to recast operators as vectors residing in a vector space. In this process of vectorization, an operator \mathcal{O} represented as a $d \times d$ matrix gets converted into a d^2 -dimensional vector $|\mathcal{O}\rangle = \text{vec } \mathcal{O} / \sqrt{d}$. There are several ways to perform this vectorization, but one way is known as row-wise or horizontal vectorization because the elements of the matrix are stacked row by row. This formulation provides a natural way to define the inner product between two operators \mathcal{O}_1 and \mathcal{O}_2 in terms of the dot product between their corresponding vectors

$$(\mathcal{O}_1 | \mathcal{O}_2) \equiv \frac{1}{d} (\text{vec } \mathcal{O}_1)^\dagger \text{vec } \mathcal{O}_2 \quad (3.4)$$

This inner product applies to systems at infinite temperature, or $\beta = 0$. The norm of an operator $\|\mathcal{O}\|$ computed using Equation (3.4) corresponds to the Frobenius norm of its matrix representation.

The Krylov space given by Equation (3.3) can be constructed using an algorithm called the Lanczos algorithm. This algorithm constructs an orthonormal basis with respect to the inner product defined above using a Gram-Schmidt-like procedure. Starting from an initial operator \mathcal{O} , the algorithm is as follows:

1. Set $|\mathcal{O}_{-1}\rangle \equiv 0$, $|\mathcal{O}_0\rangle \equiv |\mathcal{O}\rangle$, $b_0 \equiv 0$, and $n = 1$.
2. Act with the Liouvillian to produce the next state, making sure to subtract off the previous state: $|\mathcal{A}_n\rangle = \mathcal{L}|\mathcal{O}_{n-1}\rangle - b_{n-1}|\mathcal{O}_{n-2}\rangle$.
3. If $\|\mathcal{A}_n\| = 0$, stop. Otherwise, set $b_n = \|\mathcal{A}_n\|$ and $|\mathcal{O}_n\rangle = |\mathcal{A}_n\rangle/b_n$.
4. Repeat the process, setting $n \rightarrow n + 1$ and returning to step 2.

The process terminates at $n = D_K$, the Krylov dimension. The output is a D_K -dimensional orthonormal ordered basis $\{|O_n\rangle\}_{n=0}^{D_K-1} = \{|O_0\rangle, |O_1\rangle, \dots, |O_{D_K-1}\rangle\}$, called the Krylov basis. While this basis is not Hermitian, it can be made Hermitian by multiplying each element $|O_n\rangle$ by i^n .

In addition to the Krylov basis, another output of the Lanczos algorithm is a set of non-negative coefficients $\{b_n\}_{n=0}^{D_K-1}$, called the Lanczos coefficients, which completely determine the dynamics of the operator in the basis. In many applications, the Lanczos algorithm is numerically unstable due to the accumulation of rounding errors. The effect is that after a few iterations, orthogonality of the Krylov basis may be lost. To ensure orthogonality, techniques like full orthogonalization or partial reorthogonalization can be used [46].

After the Krylov basis has been constructed, it can be used to expand the operator at time t :

$$|\mathcal{O}(t)\rangle = \sum_{n=0}^{D_K-1} i^n \varphi_n(t) |\mathcal{O}_n\rangle \quad (3.5)$$

The real-valued functions $\varphi_n(t)$ are known as the Krylov-basis wavefunctions, which represent the probability amplitude for the operator at t to be in state $|\mathcal{O}_n\rangle$. From the Heisenberg equation, it can be shown that the wavefunctions satisfy the differential equation

$$\dot{\varphi}_n(t) = b_n \varphi_{n-1}(t) - b_{n+1} \varphi_{n+1}(t) \quad (3.6)$$

subject to the initial condition $\varphi_{-1}(t) = 0$ and $\varphi_n(0) = \delta_{0n}$. The dot represents a time derivative. This equation describes a single-particle hopping model, where a particle at site n hops to site $n-1$ with rate b_n and to site $n+1$ with rate b_{n+1} . The evolution of the operator is reduced to a hopping problem on a one-dimensional lattice, known as the Krylov lattice. The dynamics on the Krylov lattice are fully determined by the Lanczos coefficients.

Generically, the behavior of the Lanczos coefficients can be divided into three distinct regimes [1]. In the first regime, called the Lanczos ascent, the Lanczos coefficients grow initially until $n \sim O(S)$, where S is the thermodynamic entropy. In the second regime, called the Lanczos plateau, the coefficients plateau at $b_n \sim O(\Lambda S)$, where Λ is the energy scale. In the final regime, called the Lanczos descent, the b_n decrease at exponentially large $n \sim O(e^S)$.

According to the operator growth hypothesis, in the Lanczos ascent regime, the Lanczos coefficients should grow linearly in n for a generic chaotic system in d dimensions, with an additional

logarithmic correction in one-dimensional systems [6]. Explicitly, the hypothesis states that for a chaotic system

$$b_n = \begin{cases} \frac{An}{\log n} + O\left(\frac{n}{\log n}\right), & d = 1 \\ \alpha n + \beta + O(1), & d > 1 \end{cases} \quad (3.7)$$

where A , α , and β are constants. While the coefficients in these expressions may change for different initial operators, the pattern of linear growth should remain the same.

In general, the Lanczos coefficients need to be computed numerically, but they can be computed exactly for the SYK model when the number of interactions q is large. This can be done using the moments method, starting from the autocorrelation function $C(t) \equiv \langle \mathcal{O}(t)|\mathcal{O} \rangle$ [47]. To compute $C(t)$ in the large- q limit, an expansion in $1/q$ can be performed:

$$C(t) = 1 + \frac{1}{q}g(t) + O(1/q^2) \quad (3.8)$$

For $\mathcal{N} = 0$ SYK at infinite temperature, $g(t)$ satisfies [1, 6, 23, 48]

$$g''(t) = -2\mathcal{J}^2 e^{g(t)}, \quad \mathcal{J}^2 \equiv 2^{1-q}q\mathcal{J}^2 \quad (3.9)$$

With the initial conditions $g(0) = g'(0) = 0$, the solution is

$$C(t) = 1 + \frac{2}{q} \ln \operatorname{sech}(\mathcal{J}t) + O(1/q^2) \quad (3.10)$$

From the autocorrelation function, the moments $\mu_{2n} = C^{(2n)}(0)$ can be computed. The Lanczos coefficients can then be calculated from the moments using a recursive algorithm [47]. The result is [1, 6]

$$b_n = \begin{cases} \mathcal{J}\sqrt{2/q} + O(1/q), & n = 1 \\ \mathcal{J}\sqrt{n(n-1)} + O(1/q), & n > 1 \end{cases} \quad (3.11)$$

Comparing to Equation (3.7), $\mathcal{N} = 0$ SYK in the large- q limit satisfies the operator growth hypothesis with linear growth rate $\alpha = \mathcal{J}$.

Similar calculations can be performed for the $\mathcal{N} = 2$ SYK model. In this case, the first correction $g(t)$ satisfies [23]

$$g''(t) = -\mathcal{J}^2 e^{2g(t)} \quad (3.12)$$

which results in the Lanczos sequence

$$b_n = \begin{cases} \mathcal{J}\sqrt{1/q} + O(1/q), & n = 1 \\ \mathcal{J}\sqrt{n(n-1)} + O(1/q), & n > 1 \end{cases} \quad (3.13)$$

The leading behavior in n is unmodified, $\alpha = \mathcal{J}$. After the irrelevant deformation of Equation (2.16), the function $g(t)$ satisfies [23]

$$g''(t) = -\gamma^2 \mathcal{J}^2 e^{2g(t)}, \quad \gamma \equiv \frac{1 + \epsilon^2}{(1 - \epsilon^2)^2} \quad (3.14)$$

The overall effect is simply to replace \mathcal{J} with $\gamma\mathcal{J}$, resulting in the leading behavior $\alpha = \gamma\mathcal{J}$, which varies with the deformation strength. If the mass deformation of Equation (2.21) is applied instead, the equation for $g(t)$ becomes

$$g''(t) = -\mathcal{J}^2 \left(e^{2g(t)} + \epsilon^2 \right) \quad (3.15)$$

This equation is equivalent to that of $\mathcal{N} = 0$ SYK with q -body interactions deformed by a quadratic term, up to an overall rescaling of the coupling $\mathcal{J} \rightarrow \mathcal{J}/2$. Although an analytical solution is not known, the equation can be solved numerically or perturbatively in ϵ [31, 32].

3.2 Krylov Dimension

In Krylov subspace methods, an important role is played by the Krylov dimension D_K . Formally, D_K is the cardinality of the maximal set of linearly independent vectors in the set $\{\mathcal{L}^n \mathcal{O}\}_{n=0}^{\infty}$. One can represent these vectors in a convenient matrix form using the basis $|\omega_{ab}\rangle \equiv |E_a\rangle\langle E_b|$ formed by the eigenstates of the Hamiltonian [46]. In this basis, the n th application of the Liouvillian to the operator \mathcal{O} can be expressed as

$$\mathcal{L}^n |\mathcal{O}\rangle = \delta_{n0} \sum_{a=1}^d O_{aa} |\omega_{aa}\rangle + \sum_{\substack{a,b=1 \\ a \neq b}}^d O_{ab} \omega_{ab}^n |\omega_{ab}\rangle \quad (3.16)$$

where the phases $\omega_{ab} \equiv E_a - E_b$ are eigenvalues of the Liouvillian acting on $|\omega_{ab}\rangle$. In this basis, each vector in $\{\mathcal{L}^n \mathcal{O}\}$ can be assembled into a matrix, where the rows correspond to different values of n . The resulting matrix is a Vandermonde matrix with d^2 columns. Written out until $n = d^2 - 1$, the matrix looks like

$$\begin{pmatrix} O_{11} & O_{22} & \cdots & O_{dd} & O_{12} & O_{13} & \cdots & O_{d-1,d} \\ 0 & 0 & \cdots & 0 & O_{12}\omega_{12} & O_{13}\omega_{13} & \cdots & O_{d-1,d}\omega_{d-1,d} \\ 0 & 0 & \cdots & 0 & O_{12}\omega_{12}^2 & O_{13}\omega_{13}^2 & \cdots & O_{d-1,d}\omega_{d-1,d}^2 \\ \vdots & \vdots & \ddots & \vdots & \vdots & \vdots & \ddots & \vdots \\ 0 & 0 & \cdots & 0 & O_{12}\omega_{12}^{d^2-1} & O_{13}\omega_{13}^{d^2-1} & \cdots & O_{d-1,d}\omega_{d-1,d}^{d^2-1} \end{pmatrix} \quad (3.17)$$

The rank of this matrix is given by $\Delta(\{\omega_{ab}\}) \prod_{i,j=1}^d O_{ij}$, where $\Delta(\{\omega_{ab}\})$ is the Vandermonde determinant of the phases. The rank is zero if any of the phases are degenerate, or if any of the matrix elements of the operator in the energy basis are zero. When this happens, the corresponding columns of the matrix should be removed. Because the first d columns of the matrix are linearly dependent, $d - 1$ of them need to be removed. The Krylov dimension is then bounded by

$$1 \leq D_K \leq d^2 - d + 1 \quad (3.18)$$

It is also possible to understand the Krylov dimension in terms of the number of eigenspaces of the Liouvillian over which the operator \mathcal{O} has non-vanishing projection [46]. Suppose that, for some set of indices I , the eigenvalue of the Liouvillian is degenerate:

$$\mathcal{L}|\omega_{ab}\rangle = \omega|\omega_{ab}\rangle \quad \forall (a, b) \in I \quad (3.19)$$

Also assume that $\omega_{ab} \neq \omega$ for any $(a, b) \notin I$. Inserting Equation (3.19) into (3.16), one finds

$$\mathcal{L}^n \mathcal{O} = \omega^n \sum_{(a,b) \in I} O_{ab} |\omega_{ab}\rangle + \sum_{(a,b) \notin I} O_{ab} \omega_{ab}^n |\omega_{ab}\rangle \quad (3.20)$$

Consider the first term, which consists of the projection onto the degenerate eigenspace. With each application of the Liouvillian, the projection acquires a factor of ω . Only one of these vectors is linearly independent, and the entire eigenspace contributes one to the Krylov dimension. It follows that D_K is equal to the number of eigenspaces of \mathcal{L} over which \mathcal{O} has non-zero projection. The more degeneracies in the Liouvillian, the lower the Krylov dimension. The idea is that a chaotic system will not feature degeneracies apart from those induced by symmetries, leading to a Krylov dimension that saturates the bound of Equation (3.18).

3.3 Krylov Complexity and Entropy

An important measure of operator growth is known as Krylov complexity, which is defined as the average position of an operator in the Krylov chain

$$K(t) = \sum_{n=0}^{D_K-1} n |\varphi_n(t)|^2 \quad (3.21)$$

By definition, $K(t) \geq 0$ and it vanishes at the initial time, $K(0) = 0$. Krylov complexity grows as the operator moves away from the origin of the Krylov lattice, reflecting the fact that the Krylov basis elements are more nonlocal as the lattice index is increased. Krylov complexity can also be seen as the expectation value of the Krylov complexity operator \mathcal{K} , which is the number operator over the Krylov basis:

$$\mathcal{K}|\mathcal{O}_n\rangle = n|\mathcal{O}_n\rangle \implies K(t) = \langle \mathcal{O}(t)|\mathcal{K}|\mathcal{O}(t)\rangle \quad (3.22)$$

The full distribution of the operator provides complete information on operator growth, through higher-order moments and cumulants.

Similar to the Lanczos coefficients, the behavior of Krylov complexity can generically be divided into different regimes. In the first regime, which corresponds to the Lanczos ascent, Krylov complexity grows exponentially until the scrambling time, $t_* \sim O(\log S)$, reaching a value of $K \sim O(S)$. In the next regime, the Lanczos plateau, Krylov complexity grows linearly until the Heisenberg time, $t_H \sim O(e^S)$, reaching a value of $K \sim O(e^S)$. In this regime, the Krylov wavefunctions are uniformly distributed over the Krylov space, $|\varphi_n(t > t_H)|^2 \sim 1/D_K$. The corresponding Krylov complexity is given by $K(t > t_H) \sim D_K/2$. Krylov complexity stays at this plateau value during the Lanczos descent.

In addition to Krylov complexity, Krylov entropy also captures how randomized the distribution of Krylov wavefunctions is. It is given by

$$S(t) = - \sum_{n=0}^{D_K-1} |\varphi_n(t)|^2 \log |\varphi_n(t)|^2 \quad (3.23)$$

Like Krylov complexity, Krylov entropy increases during the ascent phase. In general, beyond the scrambling time, Krylov complexity and entropy are related logarithmically: $S(t) \sim \log K(t)$ [49].

Table 1 summarizes the growth behaviors of the Lanczos coefficients, Krylov complexity, and Krylov entropy for different types of systems. The table distinguishes between chaotic, integrable, and bounded systems. In chaotic systems, the Lanczos coefficients grow linearly, leading to exponential growth of Krylov complexity and linear growth of Krylov entropy. In integrable systems, the Lanczos coefficients grow sublinearly, αn^δ , with $\delta < 1$. This leads to sub-exponential growth of Krylov complexity and logarithmic growth of Krylov entropy. In bounded systems, which also captures the dynamics of chaotic systems at late times, the Lanczos coefficients are constant, leading to linear growth of Krylov complexity and logarithmic growth of Krylov entropy. This corresponds to $\delta = 0$ in the integrable case.

For the SYK model, Krylov complexity can be computed analytically in the large- q limit. In $\mathcal{N} = 0$, the Lanczos coefficients of Equation (3.11) can be substituted into Equation (3.6) to produce the Krylov-basis wavefunctions. Substituting the result into Equation (3.21), Krylov complexity is given by [1]

$$K(t) = \frac{2}{q} \sinh^2(\mathcal{J}t) + O(1/q^2) \quad (3.24)$$

Table 1: Comparison of growth behaviors for the Lanczos coefficients b_n , Krylov complexity $K(t)$, and Krylov entropy $S(t)$ for different system types. Chaotic systems feature linear growth of b_n , leading to exponential growth of $K(t)$ and linear growth of $S(t)$. Integrable systems exhibit sublinear growth of b_n , which leads to power-law behavior of $K(t)$. Bounded systems correspond to integrable systems with $\delta = 0$.

Quantity	System Type		
	Chaotic	Integrable	Bounded
b_n	αn	αn^δ	b
$K(t)$	$e^{2\alpha t}$	$(\alpha t)^{\frac{1}{1-\delta}}$	bt
$S(t)$	$2\alpha t$	$\log(\alpha t)$	$\log(2bt)$

which grows exponentially at early times with rate $2\alpha = 2\mathcal{J}$. For the $\mathcal{N} = 2$ model, the Lanczos coefficients of Equation (3.13) lead to

$$K(t) = \frac{1}{q} \sinh^2(\mathcal{J}t) + O(1/q^2) \quad (3.25)$$

which grows exponentially at the same rate as $\mathcal{N} = 0$. Under irrelevant deformations, the growth rate is modified to $2\alpha = 2\gamma\mathcal{J}$, where $\gamma \equiv (1 + \epsilon^2)/(1 - \epsilon^2)^2$.

4 Results

This section presents numerical results of Krylov complexity for the $\mathcal{N} = 2$ SYK model and its deformations. In Section 4.1, results for the energy degeneracy and Krylov dimension are presented. Then Section 4.2 analyzes the Lanczos sequence for various initial operators. Section 4.3 concludes with results for Krylov complexity and entropy. For the most part, the results are presented for a particular choice of system size N , but results across other values of N can be found in Appendix A. The code used to generate the results in this section and the appendices is available on the arXiv page of this paper.

4.1 Krylov Dimension

As discussed in Section 3.2, the Krylov dimension D_K is bounded by the number of eigenspaces of the Liouvillian over which a given operator has non-zero projection. The eigenvalues of the Liouvillian are the phases $\omega_{ab} \equiv E_a - E_b$ of the energy eigenvalues. Without assuming any knowledge of the operator \mathcal{O} , the maximum Krylov dimension corresponds to the number of distinct non-zero phases, plus one for the phase between identical energy levels, $\omega_{aa} = 0$.

One way this notion of the maximum Krylov dimension can be estimated is by exactly diagonalizing the Hamiltonian and counting the number of distinct phases. This method is subject to numerical errors in estimating the eigenvalues. It also requires introducing a tolerance parameter to distinguish between different phases, which is another source of numerical error. Another way to estimate the bound on Krylov dimension is to calculate the average energy degeneracy d_E , and compute the bound as

$$D_K \leq \frac{d}{d_E} \left(\frac{d}{d_E} - 1 \right) + 1 \quad (4.1)$$

This method is also subject to numerical errors, but is somewhat more robust than the previous one. In the following, this method will be used to estimate the Krylov dimension, but it was found to agree very well with the first method.

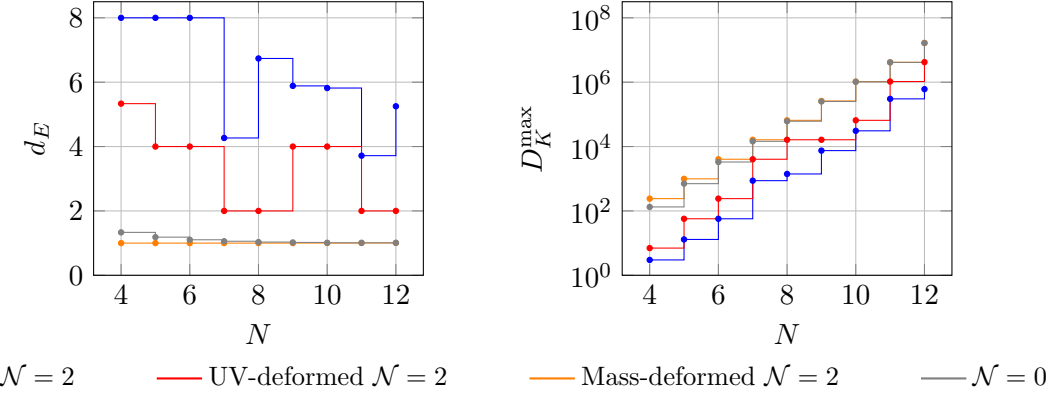


Figure 6: The average energy degeneracy d_E and bound on the Krylov dimension D_K^{\max} for $\mathcal{N} = 2$ SYK, with and without deformation. The undeformed model has a high degeneracy and low bound. After deformation, the degeneracy decreases, while the bound increases. The mass deformation has a more significant impact than the irrelevant deformation. The $\mathcal{N} = 2$ model used $q = 3$, while $\mathcal{N} = 0$ used $q = 4$. The coupling $J = 1$ was used throughout. Energies spaced less than 10^{-10} apart were considered degenerate.

Figure 6 shows the energy degeneracy and Krylov dimension bound for the $\mathcal{N} = 2$ model, with and without deformation. Also shown are results for the $\mathcal{N} = 0$ model. The number of interactions for $\mathcal{N} = 2$ was set to $q = 3$, while the corresponding number for $\mathcal{N} = 0$ was $q = 4$. The degeneracies and bounds are shown as a function of the total number of fermions N . Without deformation, the $\mathcal{N} = 2$ model has a large degeneracy, because of its enhanced symmetry. Correspondingly, it exhibits the lowest bound on the Krylov dimension. The $\mathcal{N} = 0$ model, which has less symmetry, has a lower degeneracy across all values of N . For $N = 4$, the degeneracy is $4/3$, but decreases to nearly one for large N . Its bound on the Krylov dimension is higher than that of the $\mathcal{N} = 2$ model, and is roughly exponential in the system size.

When the irrelevant deformation is turned on, the degeneracy of the $\mathcal{N} = 2$ model decreases, which increases the bound on the Krylov dimension. For $N = 4$, the degeneracy is $16/3$, but then decreases to either two or four depending on the value of N . Explicitly, for $N > 4$, $d_E = 2$ if $N \bmod 4 = 0, 3$, and $d_E = 4$ if $N \bmod 4 = 1, 2$. These degeneracies sit between the values for the $\mathcal{N} = 2$ and $\mathcal{N} = 0$ models, and are the same for all values of the deformation parameter ϵ . The corresponding bounds on the Krylov dimension lie above those for the undeformed model, but below those for the $\mathcal{N} = 0$ model.

When the mass deformation is turned on instead, the degeneracy of the $\mathcal{N} = 2$ model also decreases, but much more drastically. The degeneracy drops to one for all values of N , which agrees with the degeneracy of the $\mathcal{N} = 0$ model with $q = 2$ interactions. The bound on the Krylov dimension also increases. It is higher than that of the $\mathcal{N} = 0$ model with $q = 4$ interactions for small N , but the two agree when N is large. The Krylov bound of the deformed model matches that for the $\mathcal{N} = 0$ model with $q = 2$ interactions. It is important to note that although the bound on the Krylov dimension increases as the amount of supersymmetry is reduced, it does not imply that the model becomes more chaotic. This is because the measure for diagnosing chaos is whether the Krylov dimension for a given operator saturates the bound, not whether the size of the bound itself is small or large.

4.2 Lanczos Sequence

Using the Lanczos algorithm, the Lanczos coefficients b_n were computed starting from different initial operators for $\mathcal{N} = 2$ SYK, with and without the deformation. Three initial operators were considered. The first operator is the hopping operator, which measures transitions between fermions at different sites. Between sites i and j , it is given by

$$h_{ij} \equiv c_i^\dagger c_j + c_j^\dagger c_i \quad (4.2)$$

In this work, the hopping operator between sites at $N - 1$ and N is used throughout, but it is expected that the results will be similar for other pairs of sites. The second operator that was considered is the fermion operator at the first site, c_1 , while the third is the number operator at the first site, $n_1 \equiv c_1^\dagger c_1$.

Figure 7 shows the Lanczos sequences as the deformation strength ϵ varies. The horizontal axis employs a log scale to better visualize the initial growth. Because the irrelevant deformation breaks the various symmetries of the model, including the $U(1)$ symmetry, it is not possible to work in smaller subsectors of the Hamiltonian corresponding to a fixed charge. From a computational perspective, this effectively restricts the maximum number of fermions that could be simulated. In Figure 7, the number of fermions is set to $N = 12$, and the values $q = 3$ and $J = 1$ are used throughout. Each curve represents the average of ten Lanczos sequences, each computed from a different realization of the Hamiltonian. The shaded area around each curve represents the standard deviation of the Lanczos coefficients.

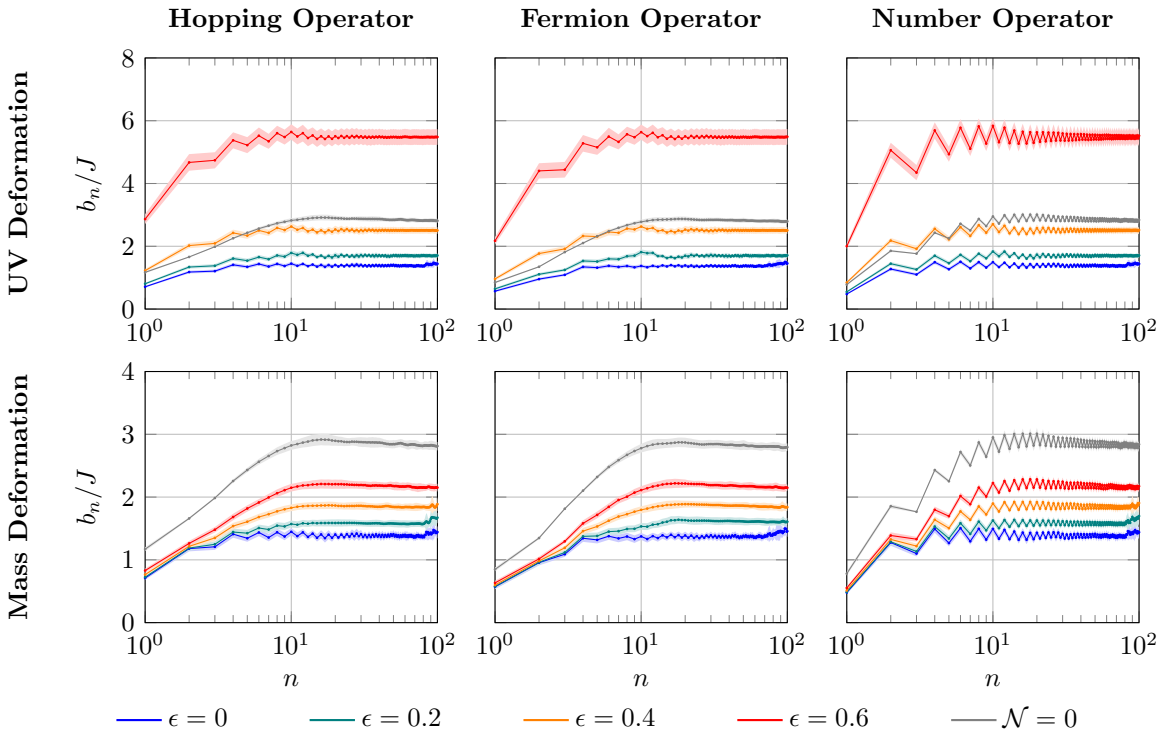


Figure 7: Lanczos coefficients b_n of $\mathcal{N} = 2$ SYK for different initial operators: the hopping operator $h_{N-1,N}$, the fermion operator c_1 , and the number operator $n_1 = c_1^\dagger c_1$. The effects of UV and mass deformations are shown as the deformation strength ϵ is varied. Each curve corresponds to the average of ten realizations of the Hamiltonian, with shaded regions indicating the standard deviation. The values $N = 12$, $q = 3$, and $J = 1$ were used throughout.

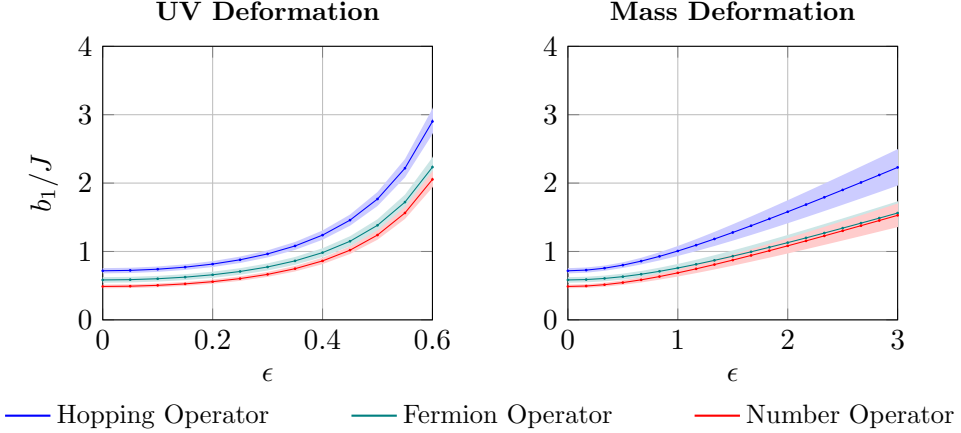


Figure 8: The first Lanczos coefficient b_1 for the hopping, fermion, and number operators for $\mathcal{N} = 2$ SYK as the deformation parameter ϵ is varied. To first approximation, b_1 provides an estimate for the growth rate α of the Lanczos coefficients, $b_n \sim \alpha\sqrt{n}$. Results are reported separately for UV and mass deformations.

The full orthogonalization version of the Lanczos algorithm was used to generate the Lanczos sequences. The number of orthogonalizations performed each iteration was set to two to mitigate numerical instabilities and ensure the orthogonality of the Krylov basis. At a regular cadence, the orthogonality matrix $G_{ij} \equiv (O_i|O_j)$ was also constructed and used to estimate the orthogonality error $\|G - I\|_2$. While the orthogonality error increased across iterations, it always remained around 10^{-14} , indicating the Krylov basis vectors remained orthogonal to a high degree.

While the Lanczos sequences tend to oscillate, their early growth is consistent with a square-root dependence, $b_n \sim \alpha\sqrt{n}$. The rate of growth α can be approximated by the first Lanczos coefficient b_1 . These coefficients are shown in Figure 8 for each initial operator and value of the deformation strength. Generally, the deformation increases the growth rate. Within the range of ϵ considered, the growth rate increases faster under the irrelevant deformation than the mass deformation. The growth rate under irrelevant deformations follows closely the expected growth rate in the large- q limit, $\alpha \sim \gamma\mathcal{J}$, even for the small value of q used here. For large values ϵ of the mass deformation, the growth rate increases linearly.

After a period of initial growth, all the Lanczos sequences begin to plateau. Under the irrelevant deformation, the Lanczos coefficients plateau within the first few iterations, $n \sim O(1)$, across all values of the deformation strength. When the mass deformation is switched on, the onset of the plateau is delayed until $n \sim O(10)$. In both cases, the plateau value increases with ϵ , which reflects the increased energy scale Λ introduced by the deformation. For reference, Figure 7 also shows the Lanczos sequences for $\mathcal{N} = 0$ SYK. Its initial growth period extends until $n \sim O(10)$, similar to IR-deformed $\mathcal{N} = 2$.

It is also possible to continue the Lanczos sequences to larger values of n , up to the eventual termination of the sequences. To accomplish this, the partial reorthogonalization version of the Lanczos algorithm was used. Appendix B reviews the differences between the full orthogonalization and partial reorthogonalization algorithms, and compares their performance on $\mathcal{N} = 2$ SYK. Figure 9 shows the full Lanczos sequences of the hopping operator for $\mathcal{N} = 2$ SYK with UV and mass deformations. The system size is $N = 8$. Without deformation, the sequence terminates after $n \sim 8,600$ iterations. Deforming the model extends the lifetime of the Lanczos sequence. Under the irrelevant deformation, the sequence terminates after $n \sim 3.2 \times 10^4$ iterations, across all values of the deformation strength. With the mass deformation, the sequence terminates after $n \sim$

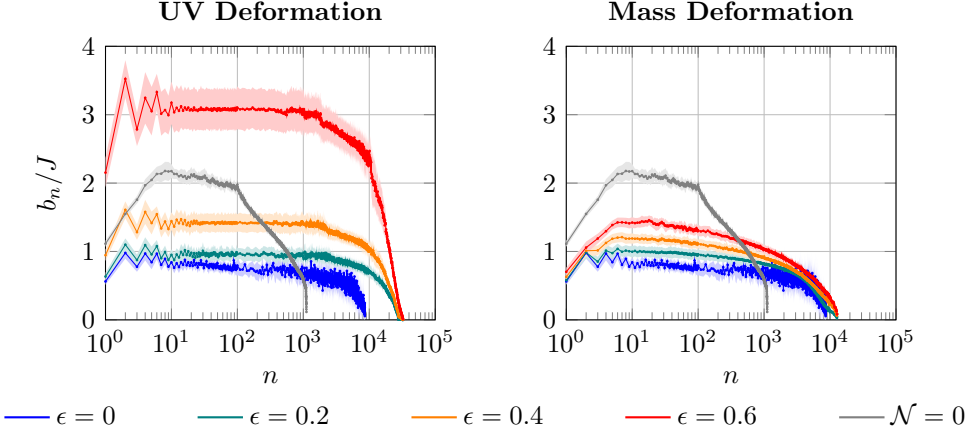


Figure 9: The complete sequence of Lanczos coefficients b_n of $\mathcal{N} = 2$ SYK for the hopping operator. Each curve corresponds to the average of ten realizations of the Hamiltonian, with shaded regions indicating the standard deviation. The values $N = 8$, $q = 3$, and $J = 1$ were used throughout.

1.3×10^4 iterations, also irrespective of the deformation strength. The duration of the plateau is also significantly smaller under the mass deformation.

The Lanczos sequences for $\mathcal{N} = 2$ SYK exhibit several interesting features absent in $\mathcal{N} = 0$ SYK. Two of these features are shown in Figure 10. In the first feature, the Lanczos coefficients oscillate between two branches, before collapsing to a single branch [50]. In the second feature, the Lanczos coefficients collapse, then split back into two branches. These features are present in single realizations of the Hamiltonian, and are not artifacts of averaging over multiple realizations. One possible explanation for these features is that they arise from the operator getting trapped in a small subspace of the overall Hilbert space. In this subspace, the operator might fail to develop large orthogonal directions, reducing the Lanczos coefficients. Once the operator escapes the subspace, the Lanczos coefficients are free to grow again.

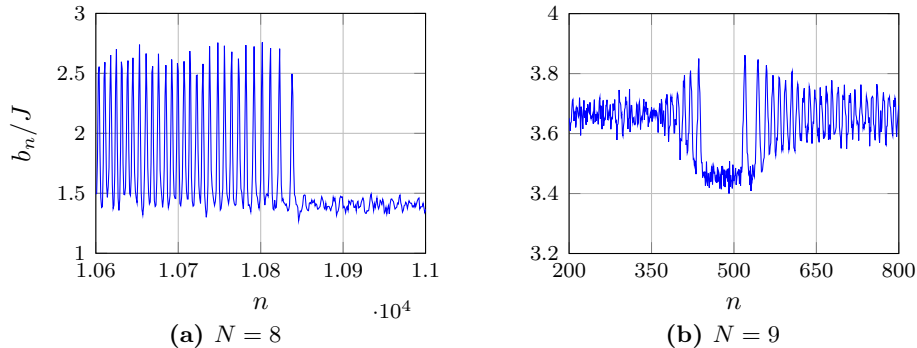


Figure 10: Two patterns in the Lanczos coefficients of $\mathcal{N} = 2$ SYK for the hopping operator: the “collapse” and “the bridge.” In the collapse, oscillations between two branches of Lanczos coefficients collapse to a single branch. In the bridge, the coefficients collapse to a single branch over a short range before splitting back into two branches. Both patterns were observed for single realizations of the Hamiltonian under the UV deformation with $\epsilon = 0.6$.

4.3 Krylov Complexity and Entropy

Once the Lanczos coefficients have been computed, the dynamics of the operator in the Krylov lattice are fully determined. Given the Lanczos sequence b_n , the Krylov basis wavefunctions $\varphi_n(t)$ were computed by integrating Equation (3.6) numerically out to $t = 10$ s, with a spacing of $\Delta t = 5 \times 10^{-4}$ s in batches of 5×10^{-3} s. The results were substituted into Equation (3.21) to compute the Krylov complexity $K(t)$, which corresponds to the average position of the operator in the Krylov lattice. This procedure was repeated for each realization of the Hamiltonian, and the results were averaged together at the very end. This quenched disorder averaging is typical in studies of Krylov complexity. If the Lanczos sequences were averaged before computing Krylov complexity, the wavepacket may not randomize efficiently before reaching the end of the Krylov lattice, which could introduce large unphysical oscillations in the complexity [46]. In the scenarios considered here, the results were not sensitive to the order of the averaging.

Figure 11 shows Krylov complexity for the different initial operators as the deformation strength is varied. The shaded area around each curve represents the standard deviation from the quenched disorder averaging. For both types of deformations, the complexity grows initially quadratically, then starts growing linearly. In the notation of Table 1, this corresponds to the Krylov exponent δ transitioning from a half to zero. The transition was observed by computing the Krylov exponent over time based on smoothed estimates of Krylov complexity, and its first and second derivatives. Appendix C discusses the estimation in more detail. The quadratic growth of Krylov complexity is a departure from exponential growth expected from chaotic systems. Initial quadratic growth has also been observed in systems with different symmetries, including SU(2) and Heisenberg-Weyl

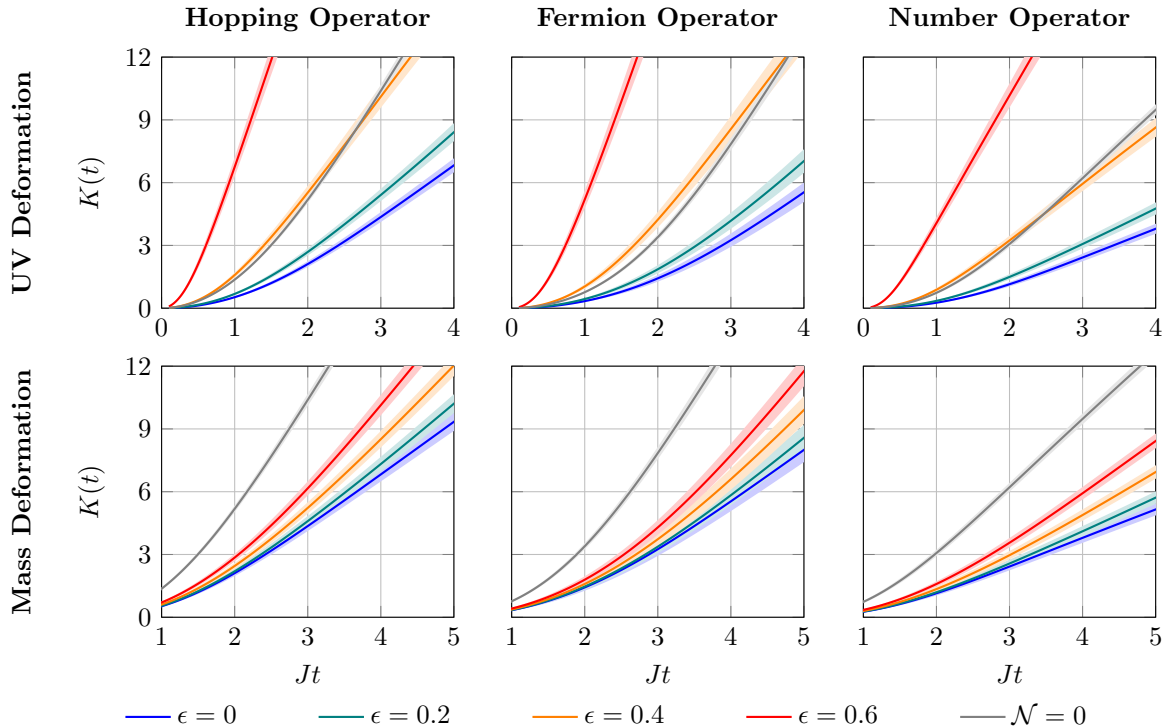


Figure 11: Krylov complexity $K(t)$ of $\mathcal{N} = 2$ SYK for different initial operators: the hopping operator $h_{N-1,N}$, the fermion operator c_1 , and the number operator $n_1 = c_1^\dagger c_1$. The effects of UV and mass deformations on complexity are shown as the deformation strength ϵ is varied. Complexity grows quadratically initially, before transitioning to linear growth. The values $N = 12$, $q = 3$, and $J = 1$ were used throughout.

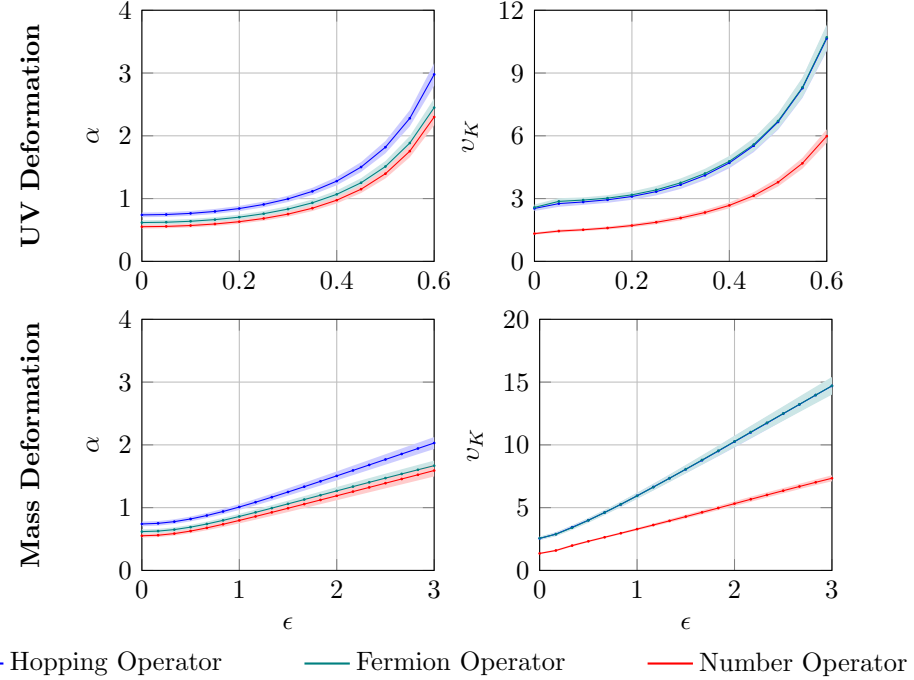


Figure 12: Comparison of Krylov complexity growth parameters for the hopping, fermion, and number operators for $\mathcal{N} = 2$ SYK as the deformation parameter ϵ is varied. Prior to $t \sim t_*$, the growth is given by a power law $K(t) \sim \alpha^2 t^2$. After t_* , complexity grows linearly, $K(t) \sim v_K t$. Results are reported separately for UV and mass deformations.

symmetry [51, 52]. Quadratic growth is also a generic consequence of working at finite N , leading to a finite-dimensional Hilbert space that can stifle the growth of the Lanczos sequence and Krylov complexity. This behavior is also observed in non-supersymmetric Majorana SYK.

Starting from estimates of the Krylov exponent, the coefficient of Krylov complexity α in the quadratic and linear phases can be estimated. The procedure is discussed in Appendix C. Figure 12 shows the growth coefficients as ϵ varies for the quadratic phase, denoted α , and linear phase, denoted v_K . For both deformations, α is consistent with the values of b_1 shown in Figure 8. For the irrelevant deformation, the curves are approximated well by $\alpha \sim 0.95\gamma$ for the hopping operator, 0.78γ for the fermion operator, and 0.74γ for the number operator. Even at the low value of $q = 3$ used here, the results agree well with α in the large- q limit, $\alpha = b_1 = \gamma\mathcal{J}$. For $q = 3$, $\mathcal{J} = 0.75$, which agrees with the results for the fermion operator. The ballistic velocity v_K also grows linearly in γ . The ballistic velocities for the hopping and fermion operators grow as $\sim 3.4\gamma$, while the number operator grows as $\sim 2.0\gamma$. Under the mass deformation, the growth coefficients α and v_K grow roughly linearly with ϵ . For the hopping operator, $\alpha \sim 0.52\epsilon$, while the fermion and number operators have $\alpha \sim 0.40\epsilon$. The ballistic velocity grows like $v_K \sim 4.4\epsilon$ for the hopping and fermion operators, while the number operator has $v_K \sim 2.0\epsilon$.

Krylov complexity can also be computed from the full sequence of Lanczos coefficients, which allows the behavior to be studied at late times. In this case, the hopping equation was integrated out to $t = 5 \times 10^5$ s with $\Delta t = 10^{-3}$ s in batches of 500 s. Figure 13 shows the full profile of Krylov complexity for the hopping operator under both UV and mass deformations for $N = 8$, plotted on a log-log scale. In this scale, the transition between quadratic and linear growth corresponds to a decrease in slope from two to one, which is discernible as an elbow in the curves. After the period of quadratic and linear growth, Krylov complexity saturates to a constant value K_{sat} at the Heisenberg

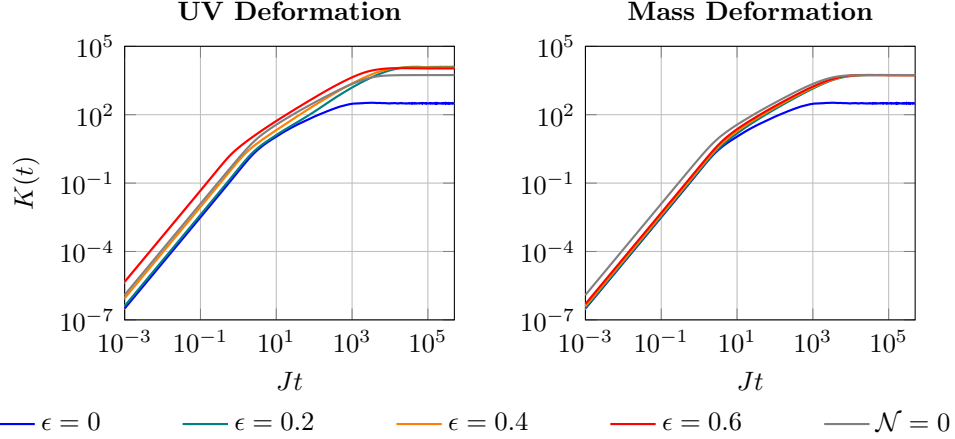


Figure 13: The complete profile of Krylov complexity $K(t)$ of $\mathcal{N} = 2$ SYK for the hopping operator. The effects of UV and mass deformations on complexity are shown as the deformation strength ϵ is varied. The values $N = 8$, $q = 3$, and $J = 1$ were used throughout.

time t_H . The undeformed model saturates at a value of 315 after 988 s. Turning on the irrelevant deformation delays the Heisenberg time, while increasing the saturation value significantly. The effect of the mass deformation is similar, but the changes are less pronounced given the range of ϵ considered. For a given value of ϵ , K_{sat} under the UV deformation is consistently larger than under the mass deformation.

Table 2 shows the Heisenberg time and saturation complexity for different deformation strengths ϵ . The saturation complexity was computed by taking the average of the last 5% of complexity values, while the Heisenberg time was computed as the time when complexity reached 95% of its saturation value. Both of these quantities are sensitive to noise and the threshold values chosen. The table also reports the saturation complexity as a fraction of the maximum Krylov dimension D_K^{\max} . The undeformed model has a D_K^{\max} of 1,407, leading to a saturation fraction of 0.22. The irrelevant deformation increases D_K^{\max} to 16,257, which leads to saturation fractions between 0.66 and 0.77. The mass deformation increases D_K^{\max} to 65,281, leading to a saturation fraction of 0.08 across all values of ϵ considered. Although the mass deformation increases the saturation complexity compared to the undeformed model, the saturation complexity is a much smaller fraction of the maximum Krylov dimension. The irrelevant deformation increases both the saturation complexity and the saturation fraction significantly.

From the Krylov wavefunctions, the Krylov entropy $S(t)$ was also computed using Equation

Table 2: Comparison of Heisenberg time t_H , saturation Krylov complexity K_{sat} , and saturation entropy S_{sat} for different deformation strengths ϵ . Results are shown separately for UV and mass deformations. Also shown are the results for $\mathcal{N} = 0$ SYK.

ϵ	UV Deformation					Mass Deformation				
	t_H	K_{sat}	$K_{\text{sat}}/D_K^{\max}$	$\log K_{\text{sat}}$	S_{sat}	t_H	K_{sat}	$K_{\text{sat}}/D_K^{\max}$	$\log K_{\text{sat}}$	S_{sat}
0.0	988	315	0.22	5.75	5.47	988	315	0.22	5.75	5.47
0.2	23,736	12,552	0.77	9.44	9.35	13,539	5,473	0.08	8.61	8.68
0.4	14,967	11,733	0.72	9.37	9.50	10,644	5,404	0.08	8.59	8.67
0.6	6,071	10,691	0.66	9.28	9.55	8,537	5,396	0.08	8.59	8.67
$\mathcal{N} = 0$	7,569	5,464	0.09	8.61	8.66	7,569	5,464	0.09	8.61	8.66

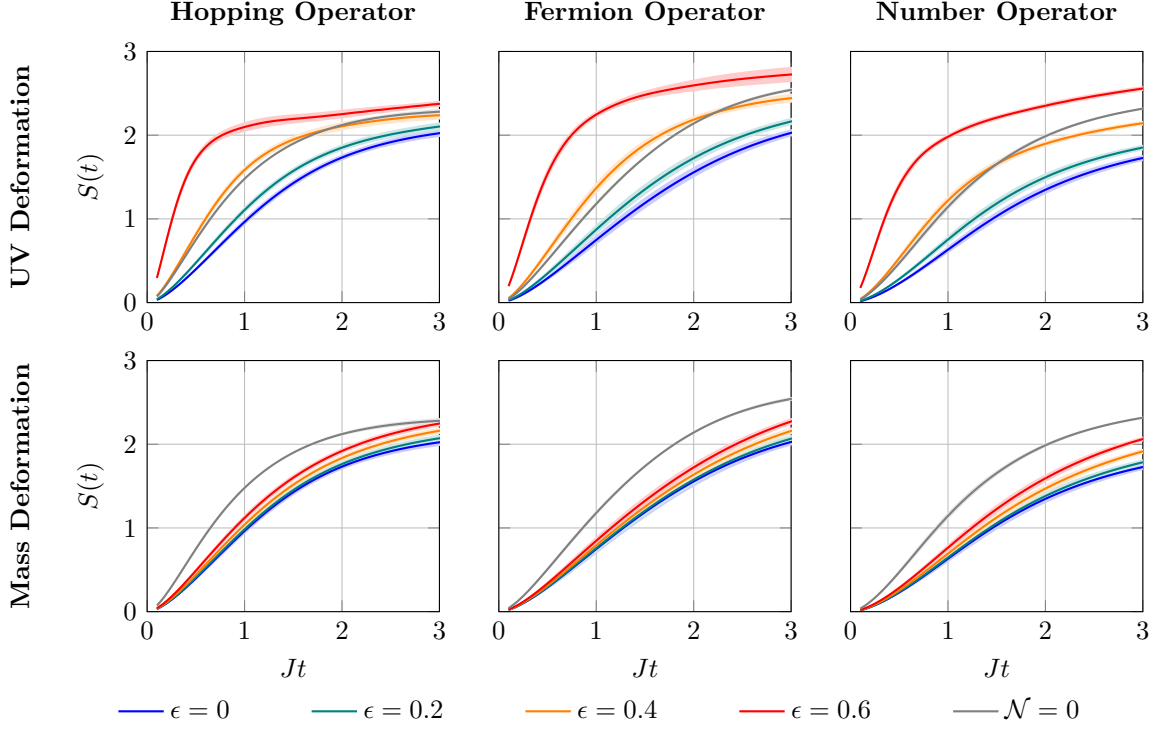


Figure 14: Krylov entropy $S(t)$ of $\mathcal{N} = 2$ SYK for different initial operators: the hopping operator $h_{N-1,N}$, the fermion operator c_1 , and the number operator $n_1 = c_1^\dagger c_1$. The effects of UV and mass deformations on the entropy are shown as the deformation strength ϵ is varied. The values $N = 12$, $q = 3$, and $J = 1$ were used throughout.

(3.23). The behavior of Krylov entropy at early times is shown in Figure 14. At early times, the wavefunction has spread out slightly from its initial value $\varphi_n(0) = \delta_{n0}$, and one can treat $\varphi_0(t)$ and $\varphi_1(t)$ as non-zero. Equation (3.6) then reduces to the system

$$\dot{\varphi}_0(t) = -b_1 \varphi_1(t), \quad \dot{\varphi}_1(t) = b_1 \varphi_0(t) \quad (4.3)$$

This gives $\varphi_0(t) = \cos(b_1 t)$, which leads to $|\varphi_0(t)|^2 \approx 1 - b_1^2 t^2$ and $|\varphi_1(t)|^2 \approx b_1^2 t^2$. The Krylov entropy is given by

$$S(t) \approx b_1^2 t^2 (1 - 2 \log(b_1 t)) \quad (4.4)$$

which is quadratic with a logarithmic correction. Although not visible in the figure, this quasi-quadratic behavior was observed in the data at very small time scales. The observed growth scales like $S(t) \sim t^{1.7}$ across all deformations, consistent with sub-quadratic growth. Fitting Equation (4.4) to the entropy at early times also gives values of b_1 consistent with those shown in Figure 8.

The full profile of Krylov entropy is shown in Figure 15. Generally, Krylov entropy grows, plateaus briefly, then continues growing before saturating at late times. Between the plateau and saturation, the entropy grows approximately logarithmically with time, which corresponds to a linear segment in the plots. The logarithmic growth agrees with the theoretical prediction of Table 1, but the entropy cannot be used to fit precise values of the growth rate α . As with Krylov complexity, the deformations increase the saturation entropy, while increasing the deformation strength reduces the saturation value. The values of saturation entropy are also reported in Table 2. Comparison with the saturation complexity shows that the saturation entropy is logarithmically

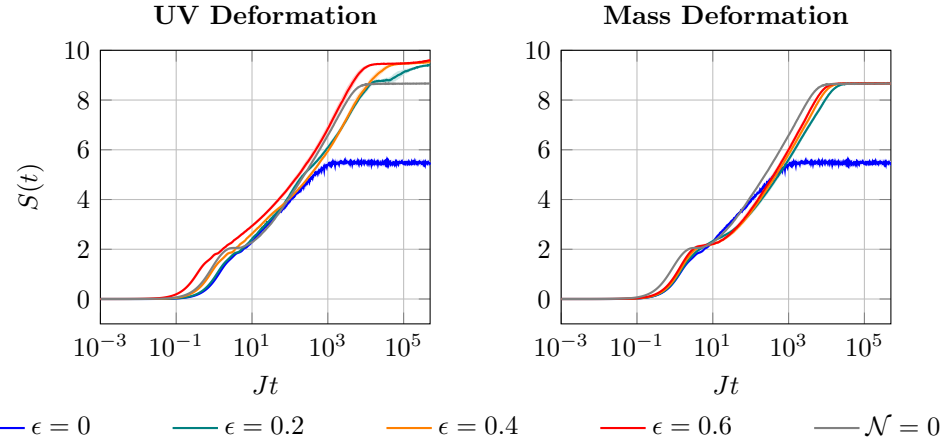


Figure 15: The complete profile of Krylov entropy $S(t)$ of $\mathcal{N} = 2$ SYK for the hopping operator. The effects of UV and mass deformations on entropy are shown as the deformation strength ϵ is varied. The values $N = 8$, $q = 3$, and $J = 1$ were used throughout.

related to the saturation complexity, $S_{\text{sat}} \sim \log K_{\text{sat}}$, consistent with the wavefunction spreading evenly across the Krylov basis at late times.

5 Discussion

This paper explored the effect of supersymmetry breaking on Krylov complexity in the $\mathcal{N} = 2$ SYK model using two types of deformations of the Hamiltonian. The first deformation was an irrelevant deformation which broke $\mathcal{N} = 2$ supersymmetry down to $\mathcal{N} = 1$, while also breaking other symmetries of the model, including $U(1)$ and $U(1)_R$ symmetries. The deformation continuously deformed the anticommutation relations between fermions, effectively rotating them relative to canonical fermions. In a holographic context, the deformation preserved the gravitational sector which occurs in the infrared. The second deformation was a mass deformation which broke $\mathcal{N} = 2$ down directly to $\mathcal{N} = 0$ through the introduction of a free Hamiltonian, while leaving other symmetries like $U(1)$ unaffected. The deformation augmented the gravitational picture by modifying the low-energy dynamics.

The effect of the deformations was first studied in terms of the energy spectrum and level statistics. The irrelevant deformation broke the BPS degeneracy, increasing the ground state energy but leaving it positive. The energy gap between BPS and non-BPS states decreased continuously with increasing deformation strength until closing at $\epsilon \approx 0.1$. The level statistics consistently exhibited a high density of closely spaced states, even at large deformation strengths. The mass deformation eliminated the BPS degeneracy and energy gap for parametrically small deformation strengths. The ground state energy became negative, consistent with a complete breaking of supersymmetry. The spectral density after the mass deformation resembled a Gaussian distribution, while the level spacings followed a Poisson distribution, similar to the $\mathcal{N} = 0$ SYK model.

Following this preliminary analysis, a Krylov subspace analysis was conducted on both deformations, which explored the Krylov dimension, Lanczos sequence, and Krylov complexity and entropy. The results are summarized as follows.

1. **Krylov dimension.** The irrelevant deformation reduced the energy degeneracy and increased the bound on the Krylov dimension, but the bound remained lower than that for

$\mathcal{N} = 0$ SYK. The mass deformation reduced the degeneracy to one, and brought the bound in line with $\mathcal{N} = 0$.

2. **Lanczos sequence.** The Lanczos coefficients exhibited an initial period of sublinear growth given by $b_n \sim \alpha n^\delta$ with $\delta = 0.5$ across both deformations and deformation strengths. The deformations increased the growth rate α . Irrelevant deformations caused the growth rate to increase as $\alpha \sim \frac{1+\epsilon^2}{(1-\epsilon^2)^2} J$, while mass deformations caused α to grow linearly in ϵ for $\epsilon \gg 1$. The deformations also extended the lifetime of the Lanczos sequence.
3. **Krylov complexity and entropy.** Krylov complexity exhibited initial quadratic growth followed by linear growth. The deformations increased the rates of quadratic and linear growth. The deformations also increased the saturation Krylov complexity and entropy, while delaying the time to saturation. The irrelevant deformation increased the saturation complexity fraction, defined as the ratio of saturation complexity to the Krylov dimension bound, while the mass deformation decreased it. The reason is that the mass deformation significantly increased the Krylov dimension compared to the irrelevant deformation, but did not increase the saturation complexity comparably.

To summarize, the impact of supersymmetry breaking on Krylov complexity of the $\mathcal{N} = 2$ SYK model depends on the specific mechanism of symmetry breaking. When supersymmetry is broken directly to $\mathcal{N} = 0$ by introducing an integrable deformation, the ratio of the saturation complexity to the size of the Krylov space decreases. In contrast, when supersymmetry is reduced to $\mathcal{N} = 1$ through an irrelevant deformation that transforms the fermionic algebra, this ratio increases. The first case drives the system toward integrability, while the second preserves its chaotic character. Notably, this distinction persists even though both deformations lead to an absolute increase in the saturation complexity and entropy.

There are several ways this work can be extended in the future.

1. **Finite temperature.** This work employed the Lanczos algorithm using an inner product that corresponds to infinite temperature. It would be interesting to repeat the analysis using a finite-temperature version of the Lanczos algorithm. Working at finite temperature naively breaks supersymmetry, but it is still possible to study the Lanczos sequence and Krylov complexity at finite temperature, which could shed light on the strong coupling regime of the theory, $\beta J \gg 1$.
2. **Other complexity measures.** This work focused on Krylov complexity, but there are other definitions of complexity, including out-of-time-order correlation functions which are characterized by the Lyapunov exponent. It would be interesting to see how the Lyapunov exponent responds to supersymmetry and its breaking in $\mathcal{N} = 2$ SYK. For example, without supersymmetry, the mass deformation causes the Lyapunov exponent to go to zero at low temperatures, while the Krylov exponent continues to be near-maximal [31]. It would be interesting to see if this behavior persists in the supersymmetric case. Other complexity measures, including circuit complexity and Nielsen complexity, can also be explored [3, 53, 54].
3. **Random matrix theory.** The results of this paper could be compared with predictions from random matrix theory [26, 55]. This could provide further insights into the universality classes of quantum chaos and complexity in deformed $\mathcal{N} = 2$ SYK.
4. **Symmetry-resolved Krylov complexity.** Another way to study the effect of symmetries on Krylov complexity is to analyze symmetry-resolved Krylov complexity, which captures

the impact each symmetry sector has on complexity [56, 57]. Generally, complexity at early times equals the average over symmetry sectors, but at late times the interplay between sectors becomes important. Symmetry-resolved Krylov complexity of $\mathcal{N} = 2$ SYK can be studied across sectors of fixed $U(1)$ or $U(1)_R$ charge. Breaking supersymmetry usually also breaks these symmetries, but it would be interesting to study the contribution of each sector to the overall complexity when supersymmetry is intact.

5. **Holographic dual.** This paper studied the quantum mechanical notion of complexity, but the most interesting area of future research would be to explore the holographic analogue of Krylov complexity in the dual gravitational system [58–62]. In a two-sided system consisting of two copies of the SYK model, the holographic dual to Krylov complexity has been interpreted as the size of the wormhole connecting the boundaries. The supersymmetric version of this picture involves super-JT gravity and the size of supersymmetric wormholes. It would be interesting to interpret the deformations of supersymmetric SYK treated here in terms of the growth of supersymmetric wormholes in the bulk.

Acknowledgments. The authors would like to thank Debarghya Chakraborty, Johanna Erdmenger, Damián Galante, Christian Northe, and Martin Sasieta for useful discussions. The authors also thank the organizers of the “Quantum Gravity, Holography, and Quantum Information” conference at the International Institute of Physics, Rio Grande do Norte, Brazil, where some of the results were presented. The work of DV is partially supported by the STFC Consolidated Grant ST/X00063X/1 “Amplitudes, Strings, & Duality.” This research utilized Queen Mary’s Apocrita HPC facility, supported by QMUL Research-IT. <http://doi.org/10.5281/zenodo.438045>.

Data access statement. The code and data used in this study are publicly available on the arXiv page of this paper.

A Complexity Results for Different System Sizes

In general, the results presented in the main text will change with system size N . This appendix contains results for the Lanczos sequences, Krylov complexity, and Krylov entropy across different system sizes. While there are a few quantitative differences, the qualitative behavior is consistent with the results presented in the main text.

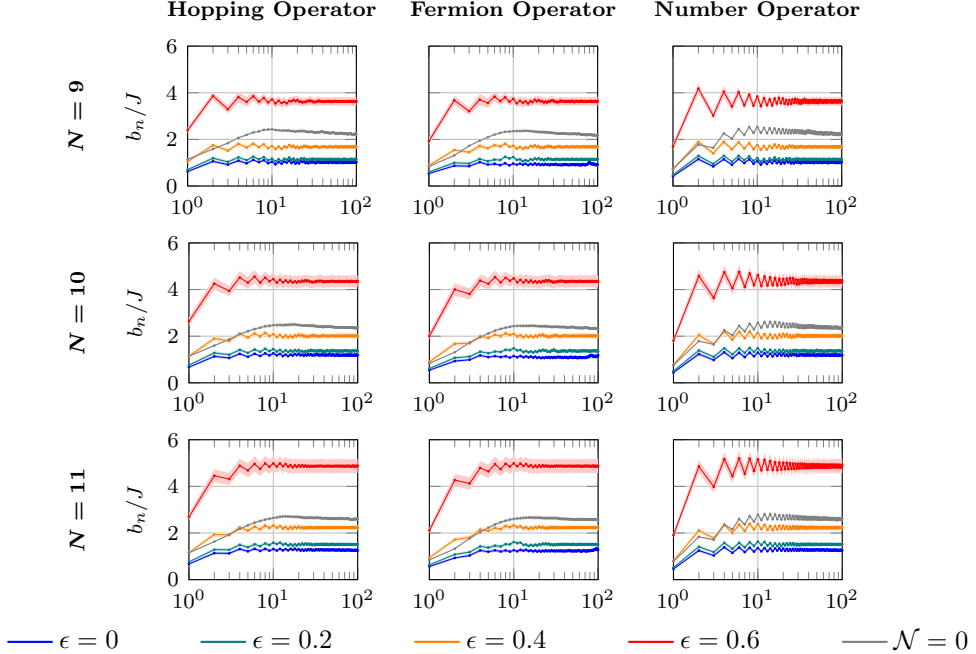


Figure 16: Lanczos coefficients b_n of $\mathcal{N} = 2$ SYK for various system sizes N as the irrelevant deformation strength ϵ is varied. The values $q = 3$ and $J = 1$ were used throughout.

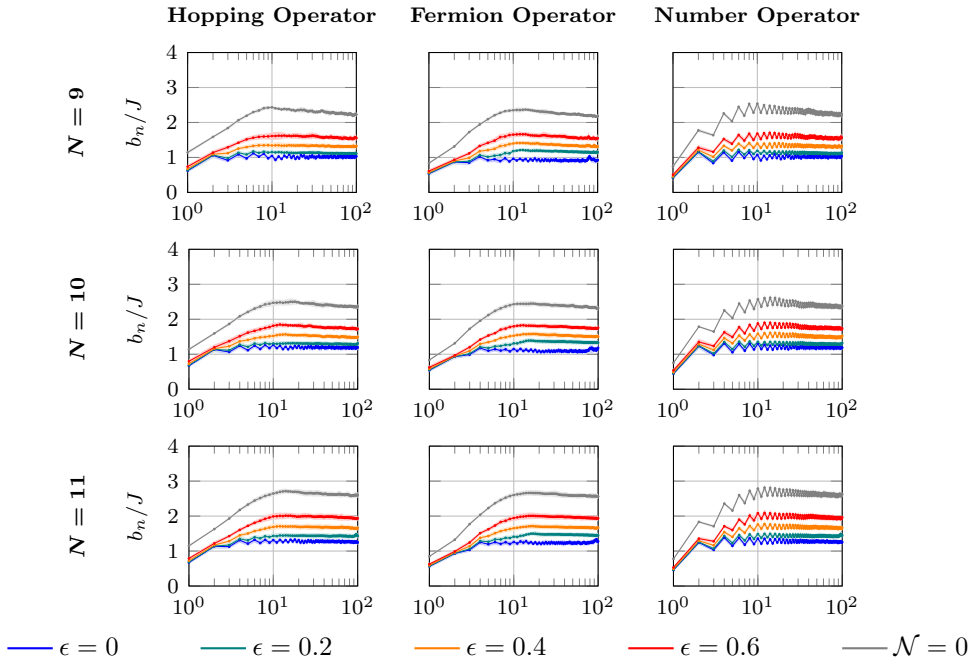


Figure 17: Lanczos coefficients b_n of $\mathcal{N} = 2$ SYK for various system sizes N as the mass deformation strength ϵ is varied. The values $q = 3$ and $J = 1$ were used throughout.

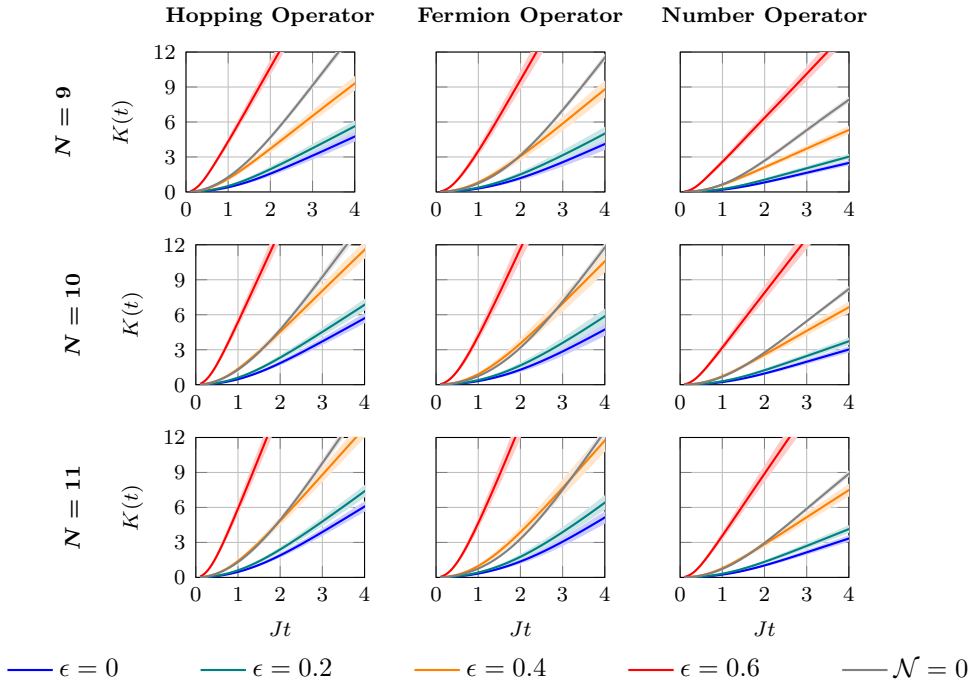


Figure 18: Krylov complexity $K(t)$ of $\mathcal{N} = 2$ SYK for various system sizes N as the irrelevant deformation strength ϵ is varied. The values $q = 3$, and $J = 1$ were used throughout.

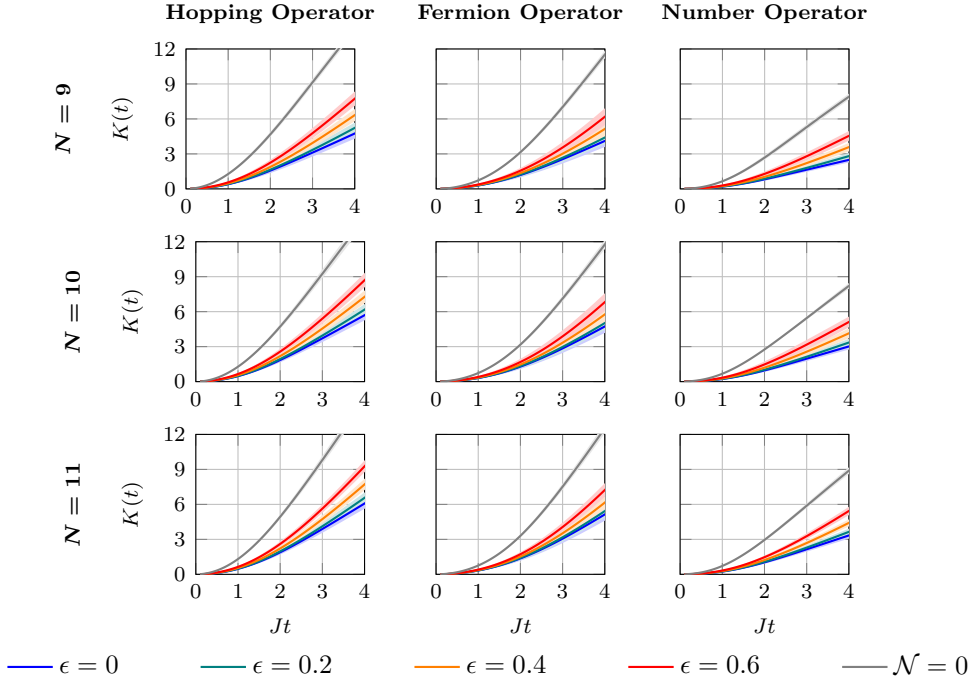


Figure 19: Krylov complexity $K(t)$ of $\mathcal{N} = 2$ SYK for various system sizes N as the mass deformation strength ϵ is varied. The values $q = 3$, and $J = 1$ were used throughout.

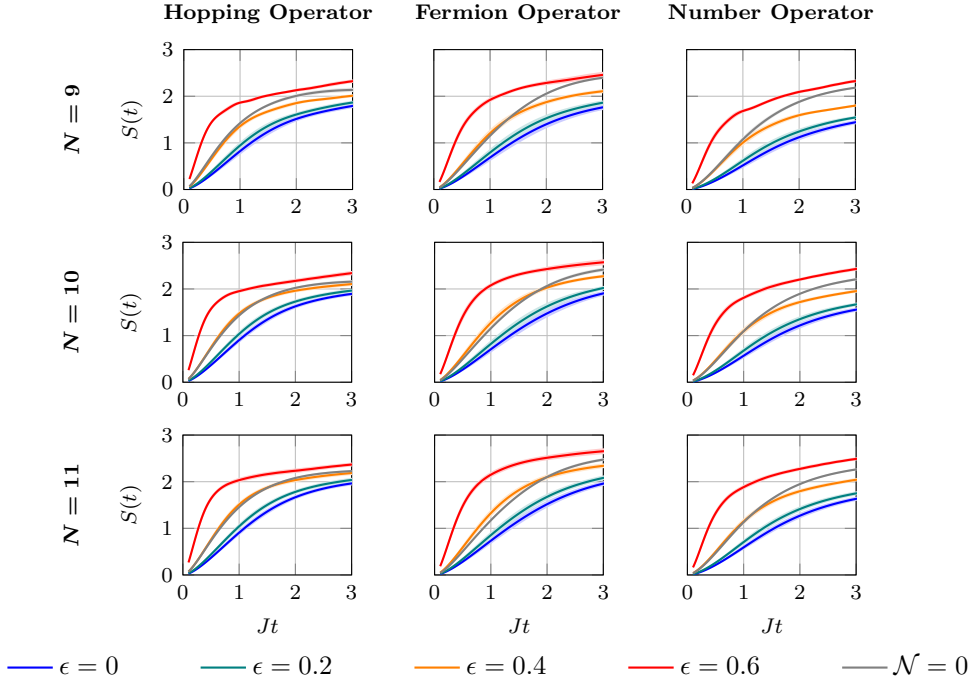


Figure 20: Krylov entropy $S(t)$ of $\mathcal{N} = 2$ SYK for various system sizes N as the irrelevant deformation strength ϵ is varied. The values $q = 3$ and $J = 1$ were used throughout.

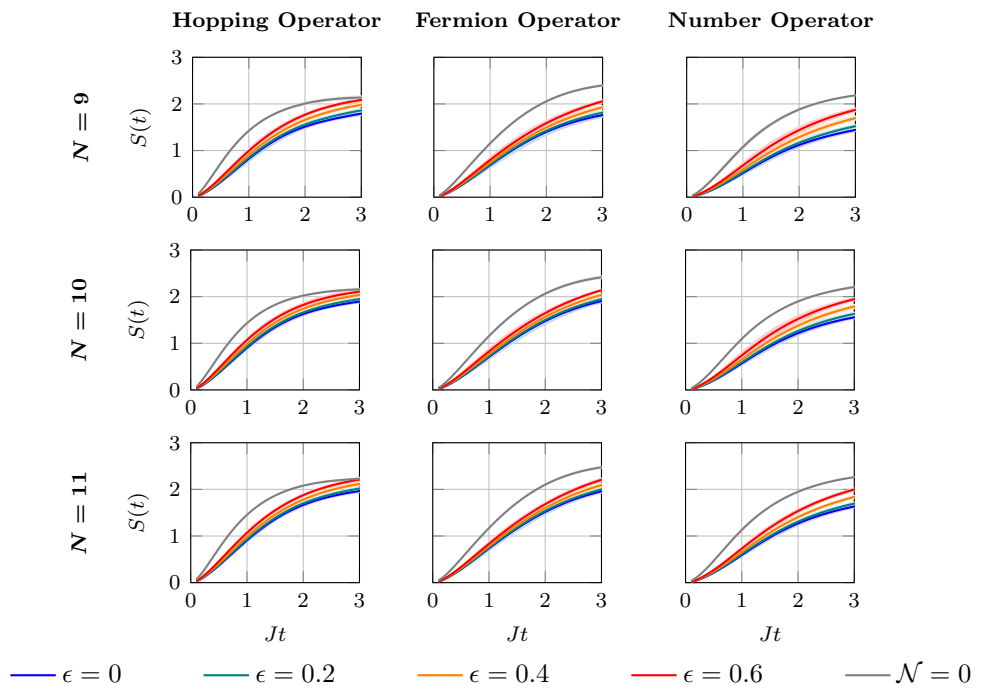


Figure 21: Krylov entropy $S(t)$ of $\mathcal{N} = 2$ SYK for various system sizes N as the mass deformation strength ϵ is varied. The values $q = 3$ and $J = 1$ were used throughout.

B Comparison of Different Lanczos Algorithms

There are two common versions of the Lanczos algorithm used in Krylov subspace methods, the full orthogonalization (FO) and the partial reorthogonalization (PRO) algorithms. This appendix summarizes the two algorithms and compares their performance in the computation of the Lanczos coefficients for the $\mathcal{N} = 2$ SYK model.

The full orthogonalization algorithm maintains orthogonality of the Krylov basis at each iteration by explicitly orthogonalizing the new basis element against all previously computed elements. The new Krylov basis element is given by

$$|\mathcal{A}_n) = \mathcal{L}|\mathcal{O}_{n-1}) \quad (B.1)$$

$$|\mathcal{A}_n) \leftarrow |\mathcal{A}_n) - \sum_{i=0}^{n-1} |\mathcal{O}_i)(\mathcal{O}_i|\mathcal{A}_n) \quad (B.2)$$

This update step replaces step two of the basic Lanczos algorithm outlined in Section 3.1, but the rest of the algorithm remains unchanged. In practice, the orthogonalization of Equation (B.2) is performed $n_O > 1$ times to ensure numerical stability. The FO algorithm is more accurate and numerically stable than the basic Lanczos algorithm, but can be computationally expensive, especially for large Krylov subspaces.

To reduce the computational cost of computing the Krylov basis, the partial reorthogonalization algorithm reorthogonalizes the new basis element only when the level of overlap with previous basis elements exceeds a certain threshold. To achieve this, PRO estimates the overlap between the n th Krylov basis element and the k th element using the recurrence relation [46]

$$W_{kn} \equiv (\mathcal{O}_k|\mathcal{O}_n) = \frac{1}{b_n} (b_{k+1} W_{k+1,n-1}^* + b_k W_{k-1,n-1}^* - b_{n-1} W_{k,n-2}), \quad k \geq 0, n \geq 2 \quad (B.3)$$

where $W_{-1,n} \equiv 0$. In this equation, the n th column of W is computed using the previous two columns, requiring only two columns of W to be stored at any time. Because the recurrence relation does not determine the overlap with the previous element $W_{n-1,n}$, the element $|\mathcal{A}_n)$ is explicitly orthogonalized against $|\mathcal{O}_{n-1})$ at each iteration. The relation also does not determine W_{nn} , but it is set to unity after normalizing $|\mathcal{A}_n)$.

If W_{kn} exceeds a predetermined threshold ϵ_P for any $k \leq n-2$, then $|\mathcal{A}_n)$ and $|\mathcal{A}_{n-1})$ are reorthogonalized against all previous elements using Equation (B.2). As with the FO algorithm, this orthogonalization step is performed n_O times. After reorthogonalization, the overlap matrix elements are set to

$$W_{ik} = \delta_{ik} + (1 - \delta_{ik})\epsilon_M, \quad \forall i \leq k, k \in \{n-1, n\} \quad (B.4)$$

The parameter ϵ_M is the machine precision of the floating point representation used in the computation, which sets the overlap between different basis elements after reorthogonalization. The advantage of the PRO algorithm is that it reduces the number of reorthogonalizations required while maintaining orthogonality of the Krylov basis to a desired level of accuracy. In practice, PRO is less accurate than FO, but significantly more efficient, allowing larger Krylov subspaces to be computed.

Figure 22 compares the FO and PRO algorithms for the computation of the Lanczos coefficients of the $\mathcal{N} = 2$ SYK model, with and without deformation. The parameters of the PRO algorithm were set to $\epsilon_P = 10^{-13}$ and $\epsilon_M = 10^{-15}$, and $n_O = 2$. The left column shows the absolute percent error in the Lanczos coefficients b_n between the two algorithms, while the right column shows the cumulative number of reorthogonalizations performed by the PRO algorithm. When $\epsilon = 0$, the

percent error is extremely small, on the order of 10^{-14} , until around $n \sim 100$. After $n \sim 100$, the error grows to around 1%, while the number of reorthogonalizations increases. After 1000 iterations, the PRO algorithm has only performed around 100 reorthogonalizations, while keeping the error to order 1%.

When the UV deformation is turned on, the PRO algorithm is able to keep the error within around 1% using only 10 reorthogonalizations, two orders of magnitude fewer than the FO algorithm. When the mass deformation is used, PRO tends to keep the error around 10^{-14} , but reorthogonalizes as much as in the undeformed case. The error is also consistently low for the $\mathcal{N} = 0$ model, with order 100 reorthogonalizations in 1000 iterations. These experiments demonstrate the effectiveness of the PRO algorithm in computing the Lanczos coefficients of the $\mathcal{N} = 2$ SYK model using significantly fewer reorthogonalizations than the FO algorithm. The FO algorithm took roughly 700–800 s to compute 1000 iterations on a MacBook Pro with M1 Pro chip and 32 GB RAM, while PRO took 500–600 s. While this is a modest speedup, it grows significantly as the number of iterations increases. Use of the PRO algorithm enabled the computation of the full Lanczos sequences for $N = 8$ reported in the main text.

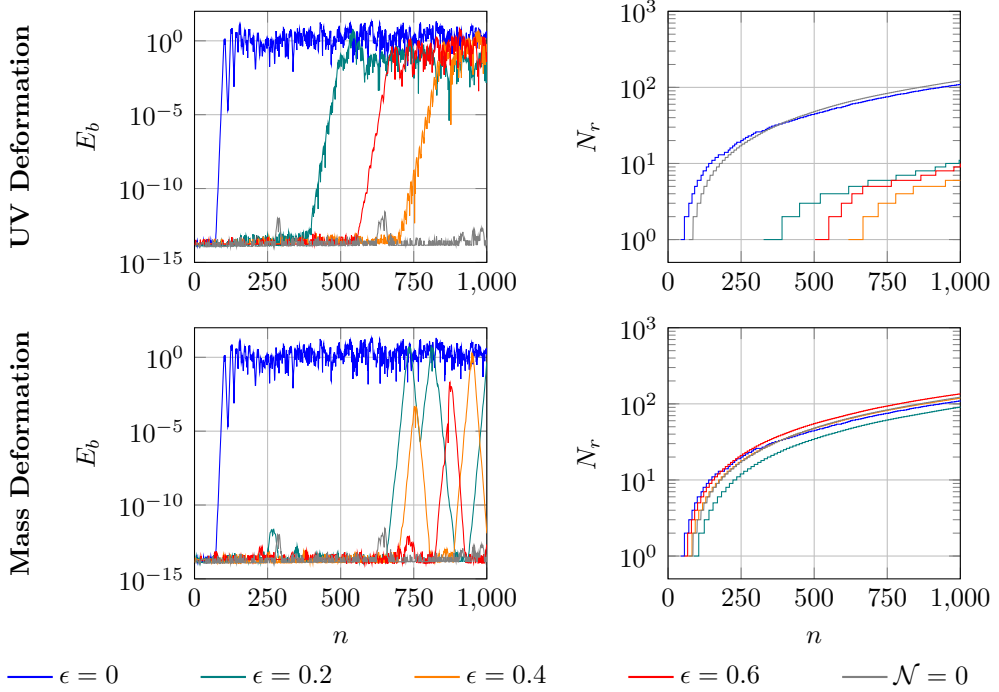


Figure 22: Percent error in the Lanczos coefficients between the FO and PRO Lanczos algorithms E_b and the cumulative number of PRO reorthogonalizations N_r as the Lanczos iteration n increases. The parameters of the PRO algorithm were set to $\epsilon_P = 10^{-13}$ and $\epsilon_M = 10^{-15}$. The number of full orthogonalizations used in both algorithms was set to $n_O = 2$. The values $N = 8$, $q = 3$, and $J = 1$ were used throughout.

C Estimation of Krylov Complexity Parameters

To analyze the growth of Krylov complexity, the various parameters characterizing the growth need to be estimated. At finite N , Krylov complexity follows power-law growth given by $K(t) \sim (\alpha t)^{\frac{1}{1-\delta}}$. One way to estimate the parameters is to use local estimates of the complexity and its derivatives. Complexity and its first two derivatives satisfy the following relations:

$$K(t) = (\alpha t)^{\frac{1}{1-\delta}} + K_0 \quad (\text{C.1})$$

$$K'(t) = \frac{(\alpha t)^{\frac{1}{1-\delta}}}{(1-\delta)t} \quad (\text{C.2})$$

$$K''(t) = \frac{\delta(\alpha t)^{\frac{1}{1-\delta}}}{(\delta-1)^2 t^2} \quad (\text{C.3})$$

This system of equations can be solved to give the parameters in terms of $K(t)$ and its derivatives:

$$\alpha(t) = \left(\frac{K'^2 t^{-\frac{K''t}{K'}}}{K' + K''t} \right)^{\frac{K'}{K' + K''t}} \quad (\text{C.4})$$

$$\delta(t) = \frac{K''t}{K' + K''t} \quad (\text{C.5})$$

$$K_0(t) = \frac{KK' - (K')^2 t + KK''t}{K' + K''t} \quad (\text{C.6})$$

In practice, $K(t)$ and its derivatives need to be smoothed to obtain reliable estimates of the parameters. Figure 23 shows estimates of $\delta(t)$ given by Equation (C.5) for various operators and deformations. Smoothing was performed using a Savitzky-Golay filter, which uses least squares to fit the data over a moving window with low-degree polynomials. The moving window was set to 0.1 seconds for the UV deformation, and one second for the mass deformation. Cubic polynomials were used for both deformations. In all instances, the exponent starts around a half, then relaxes to values around zero, which corresponds to Krylov complexity transitioning between quadratic and linear growth. The transition is not abrupt, but occurs over the course of one to two seconds, depending on the deformation. Because the transition is gradual, it is impractical to estimate a single scrambling time. In general, the irrelevant deformation advances the start of the linear growth phase. The mass deformation delays the start of the linear growth phase for small values of ϵ , but begins moving it up for larger values.

Figure 24 shows the estimates of $\alpha(t)$ given by Equation (C.4). The values of α at early times correspond to the growth rate in the quadratic phase, while the values at late times correspond to the growth rate in the linear phase, denoted v_K in the main text. Because these direct estimates can be noisy, an alternative method to estimate α and v_K was employed based on $\delta(t)$. In this method, the times at which $\delta(t)$ crosses the thresholds of 0.5 and 0 were identified. In practice, the thresholds were adjusted to account for noise in the estimates. The two crossing times define the intervals over which quadratic and linear fits to the complexity data were performed. To improve robustness, multiple fits were carried out by varying the interval endpoints, and the final estimates were taken as the averages over all fits. The results are summarized in Figure 12 of the main text.

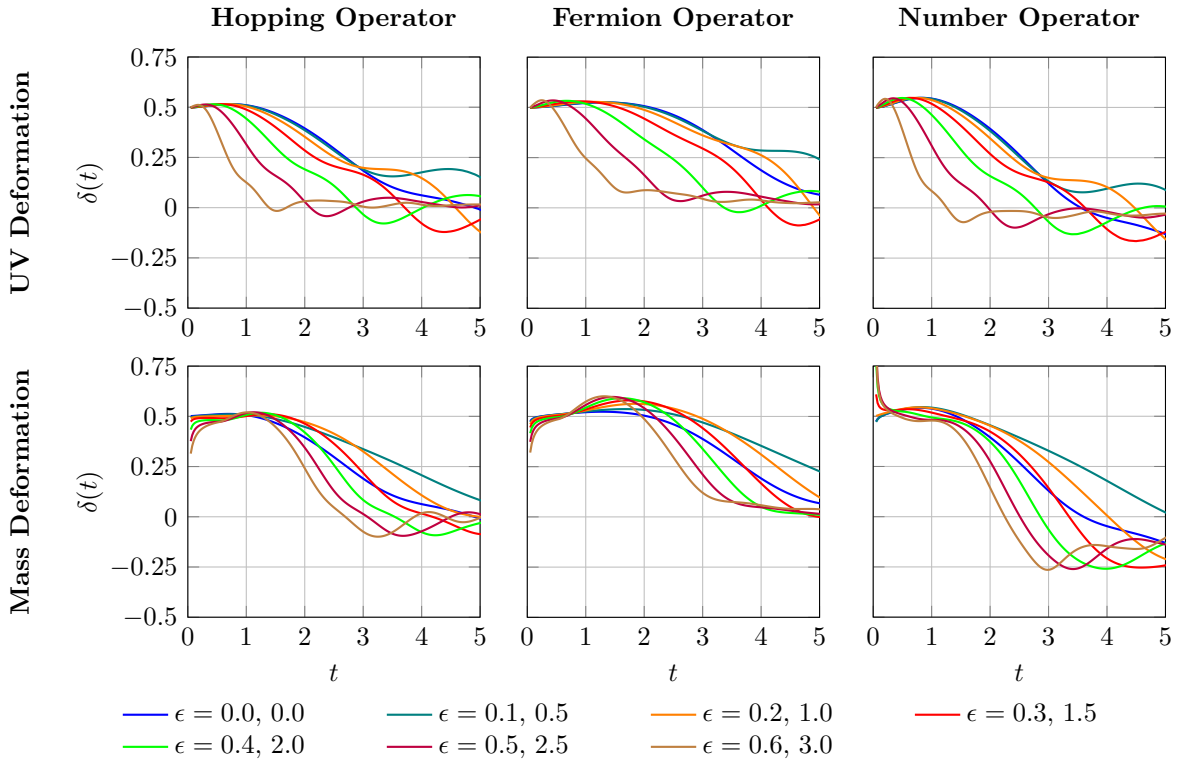


Figure 23: Krylov exponent $\delta(t)$ of $\mathcal{N} = 2$ SYK for different initial operators: the hopping operator $h_{N-1,N}$, the fermion operator c_1 , and the number operator $n_1 = c_1^\dagger c_1$. The exponent is estimated using the smoothed complexity $K(t)$ and its smoothed first and second derivatives. The effects of UV and mass deformations on the exponent are shown as the deformation strength ϵ is varied. The first value of ϵ in the legend corresponds to the UV deformation, and the second value to the mass deformation.

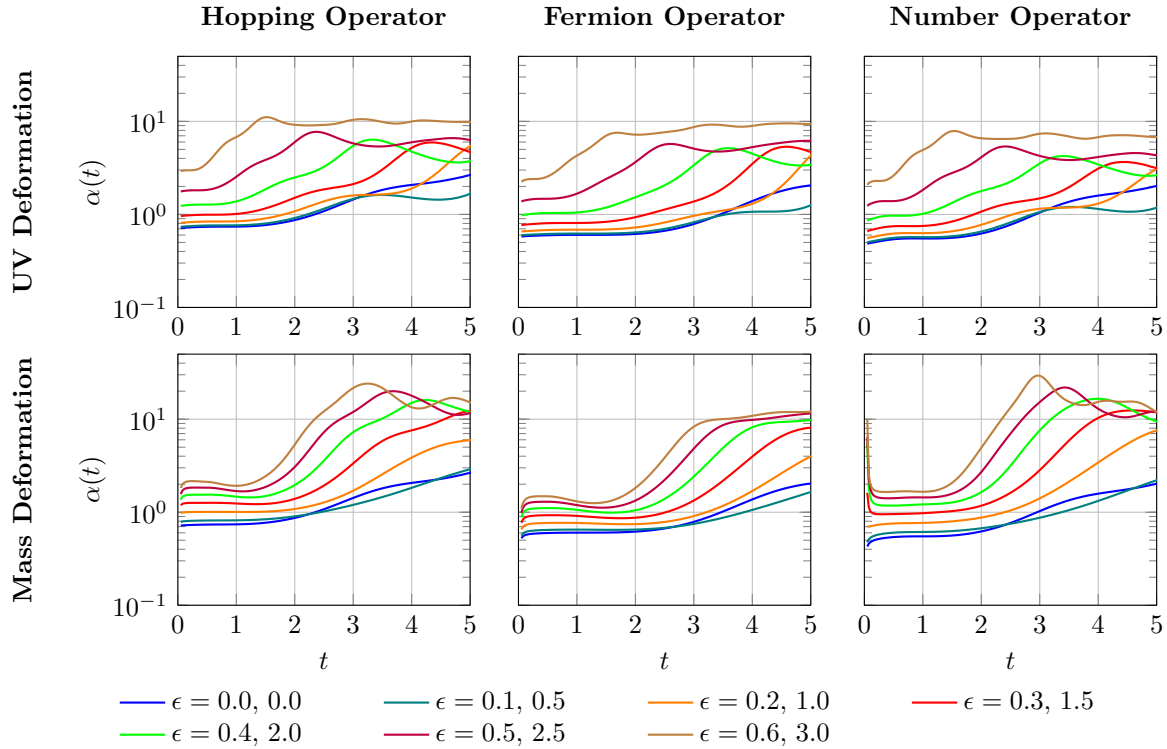


Figure 24: Krylov coefficient $\alpha(t)$ of $\mathcal{N} = 2$ SYK for different initial operators: the hopping operator $h_{N-1,N}$, the fermion operator c_1 , and the number operator $n_1 = c_1^\dagger c_1$. The coefficient is estimated using the smoothed complexity $K(t)$ and its smoothed first and second derivatives. The effects of UV and mass deformations on the coefficient are shown as the deformation strength ϵ is varied. The first value of ϵ in the legend corresponds to the UV deformation, and the second value to the mass deformation.

References

- [1] Pratik Nandy, Apollonas S. Matsoukas-Roubeas, Pablo Martínez-Azcona, Anatoly Dymarsky, and Adolfo del Campo. Quantum Dynamics in Krylov Space: Methods and Applications. *Phys. Rept.*, 1125-1128:1–82, 2024. [[2405.09628](#)].
- [2] Eliezer Rabinovici, Adrián Sánchez-Garrido, Ruth Shir, and Julian Sonner. Krylov Complexity. 2025. [[2507.06286](#)].
- [3] Stefano Baiguera, Vijay Balasubramanian, Paweł Caputa, Shira Chapman, Jonas Haferkamp, Michal P. Heller, and Nicole Yunger Halpern. Quantum Complexity in Gravity, Quantum Field Theory, and Quantum Information Science. *Phys. Rept.*, 1159:1–77, 2026. [[2503.10753](#)].
- [4] Juan Maldacena, Stephen H. Shenker, and Douglas Stanford. A Bound on Chaos. *Journal of High Energy Physics*, 2016(8), August 2016. [[1503.01409](#)].
- [5] Naoto Tsuji, Tomohiro Shitara, and Masahito Ueda. Bound on the Exponential Growth Rate of Out-of-time-ordered Correlators. *Physical Review E*, 98(1), July 2018. [[1706.09160](#)].
- [6] Daniel E. Parker, Xiangyu Cao, Alexander Avdoshkin, Thomas Scaffidi, and Ehud Altman. A Universal Operator Growth Hypothesis. *Physical Review X*, 9(4), October 2019. [[1812.08657](#)].
- [7] Jörg Liesen and Zdenek Strakos. *Krylov Subspace Methods: Principles and Analysis*. Numerical Mathematics and Scientific Computation. Oxford University Press, 2012.
- [8] Jane K. Cullum and Ralph A. Willoughby. *Lanczos Algorithms for Large Symmetric Eigenvalue Computations*. Society for Industrial and Applied Mathematics, 2002.
- [9] Subir Sachdev and Jinwu Ye. Gapless Spin-fluid Ground State in a Random Quantum Heisenberg Magnet. *Physical Review Letters*, 70(21), 1993. [[9212030](#)].
- [10] Alexei Kitaev. A Simple Model of Quantum Holography. Talks at KITP, April 7 and May 27, 2015.
- [11] Juan Maldacena and Douglas Stanford. Remarks on the Sachdev-Ye-Kitaev Model. *Physical Review D*, 94(10), November 2016. [[1604.07818](#)].
- [12] Joseph Polchinski and Vladimir Rosenhaus. The Spectrum in the Sachdev-Ye-Kitaev Model. *Journal of High Energy Physics*, 2016(4):1–25, April 2016. [[1601.06768](#)].
- [13] Antonio M. García-García and Jacobus J.M. Verbaarschot. Spectral and Thermodynamic Properties of the Sachdev-Ye-Kitaev Model. *Physical Review D*, 94(12), December 2016. [[1610.03816](#)].
- [14] Vladimir Rosenhaus. An Introduction to the SYK Model. *Journal of Physics A: Mathematical and Theoretical*, 52(32), July 2019. [[1807.03334](#)].
- [15] Micha Berkooz and Ohad Mamroud. A Cordial Introduction to Double Scaled SYK. *Rept. Prog. Phys.*, 88(3), 2025. [[2407.09396](#)].
- [16] Kristan Jensen. Chaos in AdS_2 Holography. *Physical Review Letters*, 117(11), 2016. [[1605.06098](#)].

[17] Thomas G. Mertens and Gustavo J. Turiaci. Solvable Models of Quantum Black Holes: A Review on Jackiw-Teitelboim Gravity. *Living Reviews in Relativity*, 26(1), July 2023. [2210.10846].

[18] Gustavo J. Turiaci. Les Houches Lectures on Two-dimensional Gravity and Holography. 2024. [2412.09537].

[19] Phil Saad, Stephen H. Shenker, and Douglas Stanford. JT Gravity as a Matrix Integral. 2019. [1903.11115].

[20] Wenbo Fu, Davide Gaiotto, Juan Maldacena, and Subir Sachdev. Supersymmetric Sachdev-Ye-Kitaev Models. *Physical Review D*, 95(6), March 2017. [1610.08917].

[21] Micha Berkooz, Nadav Brukner, Vladimir Narovlansky, and Amir Raz. The Double Scaled Limit of Super-symmetric SYK Models. *Journal of High Energy Physics*, 2020(12), December 2020. [2003.04405].

[22] Cheng Peng, Marcus Spradlin, and Anastasia Volovich. Correlators in the $\mathcal{N} = 2$ Supersymmetric SYK Model. *Journal of High Energy Physics*, 2017(10), October 2017. [1706.06078].

[23] Matthew Heydeman, Yifei Liu, and Gustavo J. Turiaci. Supersymmetry Breaking in SYK and the Black Hole Spectrum. *Journal of High Energy Physics*, 06, 2025. [2408.12138].

[24] M. Heydeman, G. J. Turiaci, and W. Zhao. Phases of $\mathcal{N} = 2$ Sachdev-Ye-Kitaev Models. *Journal of High Energy Physics*, 2023(1), January 2023. [2206.14900].

[25] Song He, Pak Hang Chris Lau, Zhuo-Yu Xian, and Long Zhao. Quantum Chaos, Scrambling and Operator Growth in $T\bar{T}$ Deformed SYK Models. *Journal of High Energy Physics*, 2022(12), December 2022. [2209.14936].

[26] Takuya Kanazawa and Tilo Wettig. Complete Random Matrix Classification of SYK Models with $\mathcal{N} = 0, 1$ and 2 Supersymmetry. *Journal of High Energy Physics*, 2017(9), September 2017. [1706.03044].

[27] Rathindra Nath Das, Saskia Demulder, Johanna Erdmenger, and Christian Northe. Spread Complexity for the Planar Limit of Holography. *Journal of High Energy Physics*, 06, 2025. [2412.09673].

[28] Luca V. Iliesiu and Gustavo J. Turiaci. The Statistical Mechanics of Near-extremal Black Holes. *Journal of High Energy Physics*, 2021(5), May 2021. [2003.02860].

[29] Matthew Heydeman, Luca V. Iliesiu, Gustavo J. Turiaci, and Wenli Zhao. The Statistical Mechanics of Near-BPS Black Holes. *Journal of Physics A: Mathematical and Theoretical*, 2021. [2011.01953].

[30] Dionysios Anninos, Damián A. Galante, and Sameer U. Sheorey. Renormalisation Group Flows of Deformed SYK Models. *Journal of High Energy Physics*, 11, 2023. [2212.04944].

[31] Shira Chapman, Saskia Demulder, Damián A. Galante, Sameer U. Sheorey, and Osher Shoval. Krylov Complexity and Chaos in Deformed SYK Models. *Phys. Rev. B*, 111, 2024. [2407.09604].

[32] Antonio M. García-García, Bruno Loureiro, Aurelio Romero-Bermúdez, and Masaki Tezuka. Chaotic-Integrable Transition in the Sachdev-Ye-Kitaev Model. *Physical Review Letters*, 120 (24), June 2018. [1707.02197].

[33] E. Rabinovici, A. Sánchez-Garrido, R. Shir, and J. Sonner. Krylov Complexity from Integrability to Chaos. *Journal of High Energy Physics*, 2022(7), July 2022. [2207.07701].

[34] E. Rabinovici, A. Sánchez-Garrido, R. Shir, and J. Sonner. Krylov Localization and Suppression of Complexity. *Journal of High Energy Physics*, 2022(3), March 2022. [2112.12128].

[35] Jordan S. Cotler, Guy Gur-Ari, Masanori Hanada, Joseph Polchinski, Phil Saad, Stephen H. Shenker, Douglas Stanford, Alexandre Streicher, and Masaki Tezuka. Black Holes and Random Matrices. *Journal of High Energy Physics*, 2017(5), May 2017. [1611.04650].

[36] Yingfei Gu, Alexei Kitaev, Subir Sachdev, and Grigory Tarnopolsky. Notes on the Complex Sachdev-Ye-Kitaev Model. *Journal of High Energy Physics*, 2020(2), February 2020. [1910.14099].

[37] Benjamin James Petybridge. Notes on Complex $q = 2$ SYK. 2024. [2403.04673].

[38] Ziruo Zhang and Cheng Peng. Gauging the Complex SYK Model. *Journal of High Energy Physics*, 08, 2025. [2502.18595].

[39] Subir Sachdev. Bekenstein-Hawking Entropy and Strange Metals. *Physical Review X*, 5(4), November 2015. [1506.05111].

[40] V. E. Kravtsov. Random Matrix Theory: Wigner-Dyson Statistics and Beyond. 2012. [0911.0639].

[41] Giacomo Livan, Marcel Novaes, and Pierpaolo Vivo. *Introduction to Random Matrices*. Springer International Publishing, 2018.

[42] Cheng Peng and Stefan Stanojevic. Soft Modes in $\mathcal{N} = 2$ SYK Model. *Journal of High Energy Physics*, 2021(1), January 2021. [2006.13961].

[43] Yiming Chen, Henry W. Lin, and Stephen H. Shenker. BPS Chaos. *SciPost Phys.*, 18(2), 2025.

[44] Chi-Ming Chang, Yiming Chen, Bik Soon Sia, and Zhenbin Yang. Fortuity in SYK Models. *Journal of High Energy Physics*, 08, 2025.

[45] Weam Abou Hamdan and Damián A. Galante. Exploring the Infrared Landscape of the SYK Model. 2025.

[46] E. Rabinovici, A. Sánchez-Garrido, R. Shir, and J. Sonner. Operator Complexity: A Journey to the Edge of Krylov Space. *Journal of High Energy Physics*, 2021(6), June 2021. [2009.01862].

[47] V.S. Viswanath and G. Müller. *The Recursion Method: Application to Many-Body Dynamics*. Lecture Notes in Physics Monographs. Springer Berlin Heidelberg, 2013.

[48] Daniel A. Roberts, Douglas Stanford, and Alexandre Streicher. Operator Growth in the SYK Model. *Journal of High Energy Physics*, 2018(6), June 2018. [1802.02633].

[49] J.L.F. Barbón, E. Rabinovici, R. Shir, and R. Sinha. On the Evolution of Operator Complexity Beyond Scrambling. *Journal of High Energy Physics*, 2019(10), 2019. [[1907.05393](#)].

[50] Alexander Avdoshkin and Anatoly Dymarsky. Euclidean Operator Growth and Quantum Chaos. *Phys. Rev. Res.*, 2(4), 2020. [[1911.09672](#)].

[51] Paweł Caputa, Javier M. Magan, and Dimitrios Patramanis. Geometry of Krylov Complexity. *Phys. Rev. Res.*, 4, 2021. [[2109.03824](#)].

[52] Shiyong Guo. Operator Growth in SU(2) Yang-Mills Theory. 2022. [[2208.13362](#)].

[53] Vijay Balasubramanian, Matthew DeCross, Arjun Kar, Yue (Cathy) Li, and Onkar Parrikar. Complexity Growth in Integrable and Chaotic Models. *Journal of High Energy Physics*, 07, 2021. [[2101.02209](#)].

[54] Ben Craps, Oleg Evnin, and Gabriele Pascuzzi. A Relation between Krylov and Nielsen Complexity. *Phys. Rev. Lett.*, 132(16), 2024. [[2311.18401](#)].

[55] Arjun Kar, Lampros Lamprou, Moshe Rozali, and James Sully. Random Matrix Theory for Complexity Growth and Black Hole Interiors. *Journal of High Energy Physics*, 2022(1), January 2022. [[2106.02046](#)].

[56] Paweł Caputa, Giuseppe Di Giulio, and Tran Quang Loc. Growth of Block Diagonal Operators and Symmetry-resolved Krylov Complexity. *Phys. Rev. Res.*, 7(4), 2025. [[2507.02033](#)].

[57] Paweł Caputa, Giuseppe Di Giulio, and Tran Quang Loc. Symmetry-Resolved Spread Complexity, 2025. [[2509.12992](#)].

[58] Shao-Kai Jian, Brian Swingle, and Zhuo-Yu Xian. Complexity Growth of Operators in the SYK Model and in JT Gravity. *Journal of High Energy Physics*, 2021(3), March 2021. [[2008.12274](#)].

[59] E. Rabinovici, A. Sánchez-Garrido, R. Shir, and J. Sonner. A Bulk Manifestation of Krylov Complexity. *Journal of High Energy Physics*, 08, 2023. [[2305.04355](#)].

[60] Marco Ambrosini, Eliezer Rabinovici, Adrián Sánchez-Garrido, Ruth Shir, and Julian Sonner. Operator K-complexity in DSSYK: Krylov Complexity Equals Bulk Length. *Journal of High Energy Physics*, 08, 2025. [[2412.15318](#)].

[61] Marco Ambrosini, Eliezer Rabinovici, and Julian Sonner. Holography of K-complexity: Switchbacks and Shockwaves. 2025. [[2510.17975](#)].

[62] Paweł Caputa, Bowen Chen, Ross W. McDonald, Joan Simón, and Benjamin Strittmatter. Spread Complexity Rate as Proper Momentum. 2024. [[2410.23334](#)].